Air-sea interaction processes in warm and cold sectors of extratropical cyclonic storms observed during FASTEX

By P. Ola G. Persson[1*], J. E. Hare[1], C. W. Fairall[2], and W. D. Otto[2]
[1]*CIRES/NOAA/ETL, USA*
[2]*NOAA/ETL, USA*

Accepted for Publication by
The Quarterly Journal of the Royal Meteorological Society

October 28, 2004

*Corresponding address: CIRES/NOAA/ETL, R/ET7, 325 Broadway, Boulder, CO 80305, USA
e-mail: opersson@cires.colorado.edu

SUMMARY

Mid-Atlantic measurements from the R/V *Knorr* during the Fronts and Atlantic Storm Tracks Experiment (FASTEX) are presented, and then used to examine the near-surface environment and air-sea interaction processes during the passage of 10 frontal systems. This data set includes measurements of the surface momentum, sensible heat, and moisture fluxes obtained from three different methods. The inertial dissipation (ID) drag coefficients from the R/V *Knorr* are consistent with the ID data from other measurements in open ocean storm environments. The covariance drag coefficients are generally larger than the ID ones, indicating either the presence of flow distortion problems in the covariance data or a failure of the assumptions inherent to the ID technique at these higher wind speeds. Estimates of the wind-speed dependence of the momentum, sensible heat, and latent heat transfer coefficients are based on averaged values from the two methods. These measurements 1) contribute significantly to the limited set of surface flux measurements for 10-m neutral winds in the 15-21 m s^{-1} range, 2) contain the only ship-based covariance flux measurements successfully obtained in an open-ocean, high wind speed, storm environment, and 3) include coincident wave-height measurements.

The relationships between the surface layer and the synoptic atmospheric environment is examined using composites of atmospheric and oceanic surface layer characteristics computed in 10 storms for which the *Knorr* passed through the open-wave warm sector and the cold front. These composites show minima in the sensible and latent heat fluxes and a maximum in the momentum flux just before the frontal passage during the warm-sector peak in wind speed. A second momentum flux maximum of comparable magnitude occurs in the middle of the post-frontal regime. Though the warm-sector sensible heat flux minimum is slightly negative, the sum of the two heat fluxes is positive, suggesting a positive impact on the synoptic development of these storms. Wave heights increase steadily from the eastern half of the warm sector to the frontal passage, remaining high through most of the post-frontal regime before decreasing. Differences between covariance and ID stresses are largest during the times bracketing the cold front when the wave heights and stresses are large. Differences between covariance and bulk stresses are greatest in the pre-frontal low-level jet when the frequency of waves with periods of 6-9 s maximizes and in the post-frontal regime where wind direction veers. Systematic differences between stress direction and wind direction are observed.

KEYWORDS: Observations Surface fluxes Surface layer Storm composites R/V *Knorr*

1. INTRODUCTION

Fluxes of momentum, heat, and moisture between the atmosphere and the ocean are important for climatological and synoptic processes. Direct measurements of these fluxes not only describe the air-sea interaction for that time and place, but also provide the data necessary to develop flux parameterizations for use in climate and weather forecasting models. Hence, great efforts have been made to obtain open-ocean surface flux measurements. Most of the successful air-sea flux measurement campaigns have been in the more benign tropical and subtropical low-to-medium wind speed regimes (e.g., Young *et al*. 1992; Chertock *et al.* 1993; Fairall *et al.* 1996; Fairall *et al.* 2000; Webster *et al.* 2002). A few measurement campaigns have successfully collected data in the more difficult extratropical storm environments (e.g., Large and Pond 1981, 1982; Yelland and Taylor 1996; Hauser *et al.* 2003), although the number of data points acquired at wind speeds higher than 15 m s^{-1} are limited. Furthermore, the most direct measurements are those using the covariance technique, and the number of covariance flux observations at high wind speeds are even fewer because of the difficulties involved in making such measurements in an environment with large surface waves.

Air-sea flux measurements are typically classified by stability and wind speed to make them useful for comparison to and modification of surface flux models based on Monin-Obukhov similarity theory (MOST). In this way, the dependence of the turbulent exchange coefficients on the stability and neutral wind speed can be quantified and incorporated into flux parameterization schemes. Brunke *et al.* (2003) recently compared the performance of such schemes, finding that the least problematic ones are from the Coupled Ocean-Atmosphere Response Experiment version 3.0 (COARE 3.0; Fairall *et al.* 1996, 2003), European Center for Medium-Range Weather Forecasting (ECMWF; Beljaars 1995), Goddard Earth Observing System reanalysis version 1 (GEOS-1; Large and Pond 1981, Kondo 1975), and the University of Arizona (UA; Zeng *et al.* 1998). However, classifying flux measurements with respect to physical atmospheric boundaries or regimes can provide greater physical understanding of the processes producing the flux environment and the significance of the fluxes for modifying atmospheric processes. Classifying flux data in this manner is much rarer. Large and Pond (1981, 1982) utilized time series of case studies of data collected on a mast 10 km offshore of Nova Scotia and data from the Canadian Coast Guard ship *Quadra* in the northeast Pacific Ocean to obtain physical insights into the behaviour of fluxes in relationship to atmospheric changes and to provide an assessment of errors in their flux parameterizations. Their cases showed that much of the scatter in flux measurements displayed traditionally is not random but, instead, can be physically explained by various transitions, such as changes in wind and wave directions. The flux environment provided by a change in wind direction and wind speed in one case was also utilized by Rieder and Smith (1998) to show how the surface stress measurements respond to the transitional differences between various parts of the wave spectrum. In extratropical environments, the location of fluxes with respect to frontal systems emphasizes the process by which they are generated, and can also provide insight into their significance for storm development and frontal zone modification. Modeling studies have shown that fluxes in specific regions of storms have different impacts on the storm evolution (e.g., Reed and Albright 1986; Langland *et al.* 1995).

In this paper, we first present the surface flux measurements made onboard the research vessel (R/V) *Knorr* during the Fronts and Atlantic Storm Tracks Experiment (FASTEX). Although this high wind speed data set has been used for parameterization development (Hare *et*

al. 1999) and in comparisons of flux parameterizations (Brunke *et al.* 2003), a complete description of the data collection and processing has not been formally presented. The objectives of FASTEX were to collect data relevant to the development of midlatitude atmospheric frontal waves that impact Europe (Joly *et al.* 1999). Extensive measurements of the atmospheric boundary layer structure, air-sea interaction processes, and ocean surface were obtained from four ships strategically placed in the central North Atlantic Ocean (35-65°N, 10-60°W) during January and February 1997. Two ships were specifically instrumented to make surface-layer flux measurements: the French R/V *Le Suroît*, and the U.S. R/V *Knorr*. The data from *Le Suroît* have been reported elsewhere (Eymard *et al.* 1999; Brunke *et al.* 2003), and are often referred to as the Couplage avec l'Atmosphère en Conditions Hivernales (CATCH) data set. CATCH was performed simultaneous and collocated with FASTEX. The surface-layer data from the R/V *Knorr* are the focus of this paper. The *Knorr* measurements include the only open-ocean covariance flux measurements in high wind (> 15 m s^{-1}) conditions, other than those obtained for long-fetch directions from spar buoys within 50 km of the coast (i.e., within an atmospheric Rossby radius of deformation ~ 100 km) (Smith 1980; Large and Pond 1981, 1982; Dupuis *et al.* 2003). During FASTEX, 10 to 20 storm systems passed each ship, with surface winds of 15-30 m s^{-1} associated with each passage. Hence, the FASTEX oceanic environment consisted of frequent episodes of strong winds and large waves with varying stability regimes dictated solely by the evolving synoptic conditions and ocean surface temperature.

After presenting this data set in the traditional manner in sections 2 and 3, we then use it to examine how air-sea interaction processes are modulated by the storms and how these processes in turn impact the atmospheric conditions important for the development of these storm systems, especially in the dynamically important warm sector region. Specifically, we examine the surface-layer processes occurring in the warm sector and post cold-frontal baroclinic regimes of the extratropical cyclones encountered in the North Atlantic. A compositing method is presented in section 4 to facilitate the positioning of the physical processes relative to the surface cold front, the warm sector, or the post-frontal sector of the baroclinic zone. In section 5, we discuss the atmospheric surface-layer structure and its variation relative to the synoptically modulated conditions. In section 6, we describe the ocean-surface environment and discuss the air-sea interaction, again relating these interaction processes to the synoptic structure through the compositing. A discussion of the implications of the compositing results is presented in section 7, and conclusions are presented in section 8.

2. MEASUREMENTS AND DATA PROCESSING

(a) Instrumentation

The FASTEX campaign included the deployment of 4 ships, 15-18 buoys, and 5 aircraft. The work presented here involves the data collected onboard the Woods Hole Institute of Oceanography (WHOI) 85-m R/V *Knorr*, deployed in the near upstream (NUS) area of FASTEX in the central Atlantic Ocean (Joly *et al*., 1996).

An integral part of the R/V *Knorr* deployment during FASTEX was the National Oceanic and Atmospheric Administration Environmental Technology Laboratory (NOAA/ETL) Air-Sea Interaction Group's suite of surface-layer turbulent flux instrumentation. This system has been developed during the past decade, and NOAA/ETL has deployed some form of the system on over 20 research cruises. The most vital element of the flux system is the ultrasonic anemometer/thermometer (Gill-Solent, R2), which samples at over 20 Hz. Also of critical value

to the measurement system is a fast-response infrared hygrometer (Ophir, IR-2000), which provides in situ measurements of small-scale humidity fluctuations. Both of these instruments have proven to be rugged enough to withstand months in the harsh marine environment (Hare *et al.* 2000). During FASTEX, these instruments were mounted at the top of a sturdy, reinforced, pivoting, 12.5 m mast placed 3 m to the rear of the bow [Fig. 1(a) and Fig. 1(b)], allowing the collection of data with minimal flow distortion whenever the bow was pointed into the wind. The sensors were 15.5-19.2 m above the nominal water line. The hygrometer optics were cleaned with a remotely operated water spray when the data indicated that salt accumulation had become significant (Fairall and Young 1991). Shipboard, direct covariance measurements of turbulent fluxes were possible from this system because of the routine application of a platform motion measurement package (Systron-Donner, Motion-Pak) and a motion correction algorithm (Anctil *et al.*, 1994; Edson *et al.* 1998). The Motion-Pak consists of a slender package of 3-axis accelerometers and rotation rate sensors mounted in a canister in close proximity to the sonic anemometer. Details on the turbulent flux instruments and on the process for platform-motion correction can be found in Edson *et al.* (1998) and Fairall *et al.* (1997).

Mean sensors included in the ETL suite are air temperature and humidity (Väisälä HMP35) mounted on the bow mast, floating sea-surface temperature (SST) thermistor often referred to as the "sea snake," and infrared and solar radiative flux sensors (Eppley PIR and PSP, respectively). The WHOI improved meteorological (IMET) instruments (described at http://www.whoi.edu/marops/research_vessels/knorr/sciequip_instrument.html) were mounted on a yardarm of the foremast located in front of the bridge [Fig. 1(a)]. The IMET data, along with the ship navigation data, were distributed every 2 seconds by the onboard Athena data system, were often redundant, and helped fill gaps in the ETL data stream. Additional digital input to the data acquisition system included a gyroscopic compass and a GPS receiver, deployed to monitor the ship maneuvers. This integrated flux system enables the estimation of the turbulent fluxes of latent heat, sensible heat, and momentum using three established techniques: the direct eddy correlation (same as covariance), inertial-dissipation (ID), and bulk aerodynamic methods.

Other systems deployed on the *Knorr* provided critical information about the ocean surface and boundary-layer environment. A T. S. K. Corporation microwave wave-height meter (described at http://www.tsk-jp.com/tska/index.html) provided by the Bedford Institute of Oceanography was deployed on the bow of the *Knorr* to measure wave statistics at a rate of 2 Hz. This instrument included the downward-looking Doppler radar with a 13° beam width, which sampled a 1.8 m diameter footprint of the ocean surface from its location at the end of a short bowsprit [Fig. 1(a)], and a gimbaled vertical accelerometer mounted below decks at the bow on the ship's centerline. The ETL floating thermistor and the ship intake provided two in-situ measurements of the SST. In addition, subjective estimates of sea-surface conditions, including wave and swell heights and directions, were provided by the ship’s crew from the bridge at least every four hours. Precipitation was measured using an National Center for Atmospheric Research (NCAR) optical raingauge and a University of Kiel gimbaled ship raingauge [Fig.1(a)]. Other in-situ and remote sensors not essential for this study but present on the R/V *Knorr*, such as the Omega rawinsondes and vertically pointing Doppler S-band radar (White *et al.* 2000), are listed in Table 1. This ship-based observation system provides detailed depictions of the atmospheric boundary and surface layers and the ocean surface, all of which are essential to describing the influence of air-sea interactions on the genesis and development of the FASTEX storms.

(b) Data processing

This study uses data from four main sources: the ETL motion-corrected flux package, the ship's Athena system, the ETL mean measurement systems, and the TSK wave-height recorder. The first three produce the surface fluxes and the mean values. The last one produces the wave-height and wave period data. Descriptions of the processing of the surface fluxes, the bulk meteorological data, and the TSK wave-height data follow. The processed data sets are available from ftp://ftp.etl.noaa.gov/et7/anonymous/cfairall/fluxdata/fastex/ or the FASTEX data archives (http://www.cnrm.meteo.fr/dbfastex/).

(i) Surface fluxes. After the velocity signals are corrected for ship motion, data from the first three sources are combined to produce a set of 10-minute processed data files, which include statistics, spectra, and means of all fast-response signals and the mean meteorological and SST variables. We choose 10-minute segments in order to minimize the effects of weakly non-stationary conditions on the statistics. A final routine applies various corrections, computes the ID and bulk fluxes and the data-quality indices, and writes the final file of 10-minute averages. This program also averages the data to fixed 1-hr time intervals and computes the ID and bulk fluxes from 1-hr means. The hourly averages provide a more stable estimate of the variances and turbulent fluxes.

Conditional sampling criteria are used to ensure that only high quality products are included in the subsequent analysis. For each 10-minute period, data are retained only if a) the relative wind direction is less than ± 45° from directly onto the ship bow, b) the standard deviation of the ship's heading is less than 8°, c) the standard deviation of the ship's speed over ground is less than 2 m s^{-1}, d) the standard deviation of the cross-ship motion correction is less than 2 m s^{-1}, and e) the rainfall rate is less than 5 mm h^{-1}. Criterion d) ensures the quality of the platform motion corrections. There are additional requirements on the vertical velocity variance and the cross-stream velocity variance. These criteria are rather weak, allowing some outliers to remain. After conditional sampling, a total of 220 hours of quality flux data remain within 10-minute segments. Only 10-min data passing the quality control checks were used in producing the 1-hr averaged turbulence variables (e.g., covariances, variances, structure function parameters).

The covariance turbulent fluxes are computed by converting the anemometer 3-component velocities to fixed earth coordinates, correcting the fast time series for ship motion, and rotating the coordinate system to be aligned along the 10-min mean flow. The covariance stress (τ_c), sensible heat flux (H_{sc}) and latent heat flux (H_{lc}) are then computed from

$$\tau_c = \tau_{sc} = \rho_a u_*^2 = -\rho_a (\overline{u_s' w'}); \tag{2.1}$$

$$\tau_{cc} = -\rho_a (\overline{u_c' w'}); \tag{2.2}$$

$$H_{sc} = -\rho_a c_p u_* t_* = c_p \rho_a \overline{T' w'} = c_p \rho_a [\overline{T_{sn}' w'} - 0.51\, T\, \overline{q' w'}] \tag{2.3}$$

$$H_{lc} = -\rho_a L_e u_* q_* = L_e \rho_a \overline{q' w'}, \tag{2.4}$$

where u_s is the wind component in the mean wind direction (streamwise component), u_c is the cross-stream wind component, w is the motion-corrected vertical velocity, T is the mean air

temperature, T_{sn} is the sonic temperature, q is the specific humidity, ρ_a is the air density, c_p is the heat capacity of air at constant pressure, L_e is the latent heat of vaporization, u_* is the friction velocity, and t_* and q_* are the scalar flux scales for temperature and humidity, respectively. Primes indicate turbulent departures from the mean. Note that the covariance stress, τ_c, is defined as the streamwise stress, τ_{sc}, and does not include a contribution from the cross-stream covariance stress, τ_{cc}.

For H_{sc}, the humidity contribution to the sonic temperature (second term on rhs of 2.3) was removed using the bulk latent heat flux (H_{lb}) computed from the COARE3.0 scheme (Fairall *et al*., 1996, 2003) to estimate $\overline{q' w'}$. To remove effects of transducer delay, only times were used for which the temperature spectra showed a -5/3 slope at high-frequencies, thereby reducing the amount of sensible heat flux data compared to the momentum flux data. The H_{sc} showed non-zero values when the air-sea temperature difference was near zero. Examination of the covariance spectra to idealized spectra as a function of wind speed for these cases suggested that a combination of motion correction errors and flexing of the sonic anemometer produced these unrealistic values. Therefore, a bias correction which increased with increasing wind speed was applied to all the H_{sc} data presented in this study. This correction was determined from the heat flux offset from zero at near-zero air-sea temperature differences. At a wind speed of 20 m s^{-1}, this correction reduced H_{sc} by about 9 W m^{-2}.

For H_{lc}, the fast humidity fluctuations from the IR hygrometer were scaled by the ratio of the mean hygrometer humidity to the mean IMET humidity (i.e., increased by about 9%) for use in computations of the $\overline{q' w'}$ covariance and the standard deviation of humidity fluctuations. Using Kristensen *et al.* (1997), an additional scaling factor (1.0% increase) for the $\overline{q' w'}$ covariance was used to account for the physical separation of the hygrometer and the sonic anemometer, as the latter was 1.6 m above the former. Because the IR hygrometers detect water-vapor mass concentration, the H_{lc} are also corrected as per Webb *et al.* (1980).

Averaging the three components of the mast accelerometers for selected time periods during the cruise provides an estimate of the mean tilt of the mast with respect to the gravitational vector. This analysis shows that the mean tilt of the mast is toward the aft approximately 2° and to the port side about 1°. Flow tilt angles, determined from the sonic-measured mean vertical and streamwise velocities averaged with respect to the relative wind direction, varied from 7° to 10° from the horizontal. Experience has indicated that mean streamwise flow tilts greater than about 15° give questionable fluxes. Furthermore, these observed flow tilt angles are significantly greater than the 2.3° flow tilt angle for bow-on winds obtained from model flow distortion studies of the R/V *Knorr* (Yelland *et al.* 2002; Moat and Yelland 1998), suggesting that the true flow distortion may be greater than the modeled one. Therefore, we have estimated that the mean wind speed at the sonic anemometer location is decreased by about 4.5% rather than the 0.85% estimated by the modeling studies. This increase in airflow deficit of 3.65% may have resulted because the model study was unable to represent the bow mast (referred to as the lattice tower in the modeling studies) and the instrumentation on this mast, and is consistent with the mast and instrumentation effects on the R/V *L'Atalante* seen by Weill *et al.* (2003) in computational fluid dynamics and physical simulations.

Furthermore, other studies have suggested that the flow distortion may vary significantly with relative wind direction (e.g., Dupuis *et al.* 2003). In an attempt to quantify this effect for the R/V *Knorr*, we chose 21 periods where the non-bow-on winds were interspersed with the bow-on winds, and performed polynomial regressions using only the bow-on (±10°) winds to

obtain "correct" winds during the times of non-bow-on winds. Though this procedure led to differences with a substantial scatter, the bin mean of these differences showed a nearly linear increase from 0% for bow-on winds to 3% at 35°. That is, the flow accelerated as it moved away from the bow. This 3% acceleration at 35° is about half that reported by Dupuis *et al.* (2003) using a simulation of the R/V *L'Atalante* and is consistent with those estimated from "star" ship patterns for the R/V Ron Brown (Webster *et al*. 2002), a vessel with a similar shape to the R/V *Knorr*. More than 96% of the "good" data from the R/V *Knorr* used in this paper has relative wind directions within the range -12.5° - +32.5°, centered near +10° (just to the right of the bow when viewing the bow from the ship). The wind speeds are corrected for this relative wind direction effect, retaining the 4.5% mean correction for all directions used. That is, bow-on winds were increased by about 5.5% while winds with relative directions of ±35 degrees were increased only 2.5%. The data set has also been corrected for a 0.7 m upward flow displacement at the bow mast for all relative wind directions as estimated by Yelland *et al.* (2002). These corrections for wind speed errors and vertical displacement affect primarily the ID fluxes and the mean winds. As flow-distortion effects on the turbulent eddies are unknown, no corrections were applied to the covariance statistics.

To compute the ID fluxes (τ_{ID}, H_{sID}, H_{lID}), the slope of each power spectrum within a reasonable range of inertial-subrange frequencies is compared with the canonical -5/3 power law, and the spectral level within that narrow range of frequencies is used to compute the relevant structure function parameter. It is then straightforward to compute ID estimates of the turbulent scaling parameters for velocity (u_*), temperature (t_*), and humidity (q_*) (see Fairall and Larsen 1986).

We normally use the clear channel counts from the IR hygrometer as an index of clean optics. Past experience has indicated that the absolute calibration of the IR hygrometer is degraded as the optics become contaminated with salt and/or water. With clean optics the mean clear channel counts are around 2800-3000 and the standard deviation is between 2-15. In experiments with predominantly calm weather we reject humidity flux values when the mean counts are below 2500 and/or the standard deviation is above 20, although a threshold of 50 often provides acceptable data. FASTEX had predominantly stormy weather, so those criteria reject the majority of the data. To estimate the contamination effects on the fluxes, we did a linear regression of H_{lc}/H_{lb} (or H_{lID}/H_{lb}) vs. mean clear channel counts for latent heat flux. For the covariance flux, there is a positive slope and the ratio is 1.0 for mean counts greater than 2800; for the ID flux, the slope is negative and the ratio is 1.05 for mean counts greater than 2800. Therefore, we have used these slopes to adjust the H_{lc} and H_{lID} for mean counts <2800. At a mean clear channel count of 2000, this amounts to a 15% increase in H_{lc} and a 19% decrease in H_{lID}. While an adjustment of this type violates the usual policy of never adjusting or rejecting direct flux values based on their agreement with the bulk model, we have accepted this compromise because it has essentially no effect on the average of the covariance and ID fluxes (i.e., they are adjusted in opposite directions). Users who find this adjustment overly objectionable can restrict their analysis to data with the standard deviation of clear channel counts less than 20. An unadjusted version of the data set is available on request.

(ii) Bulk meteorological data. True wind speed is computed from the sonic anemometer using the ship's Laser ring gyro and the GPS speed over ground and course over ground; thus, it is interpreted as the speed relative to the fixed earth. Air temperature and humidity from the ETL system and the ship's IMET T/RH sensor were carefully compared with a handheld wet/dry bulb

psychrometer during the experiment. Based on these intercomparisons, the IMET values were deemed more accurate and provide the mean T and q values used in this study. At various times during the cruise the sea snake was removed from the water, in which case data from the ship's thermosalinograph were substituted. Thermosalinograph SST measurements were generally of lower quality due to the rough conditions which caused the intake port to occasionally come out of the water [an example of bad thermosalinograph data can be seen in Fig. 11(c) near JD 8.95].

The longwave radiative flux from the Eppley PIR unit was logged and computed, as per Fairall *et al.* (1998). The rain rate from the NCAR optical raingauge was used, as it appeared to be less affected by airflow over the ship's bridge. However, data were only available after 2350 UTC January 9. Prior to that time, values from the Kiel ship gauge are used, though the location of the Kiel gauge [see Fig. 1(a)] apparently led to underestimates of the precipitation amounts by a factor of 3-10 compared to the NCAR gauge. Hence, the editing of the surface fluxes as described above may not have removed all rainfall-contaminated cases before January 9.

(iii) TSK wave-height data. By vertically integrating the Doppler signal every 0.5 sec, the TSK microwave wave-height meter provided an objective measurement of the height between the instrument and the ocean surface (see Fig. 1a), internally corrected for vertical accelerations. One-hour time series of height are scanned to identify the local troughs and crests (Fig. 2). The height of an individual wave is computed as the mean of the differences between two consecutive troughs and the intervening crest. The measured wave period (encounter period) (T_{wm}) is defined as the time between the troughs. To get the true wave period (T_w), T_{wm} must be corrected for horizontal ship speed (speed-over-ground, SOG) and the relative angle between the ship's course-over-ground (COG) and the waves' phase velocity direction (ϕ_w) using

$$T_w = 0.5*[T_{wm} + \{T_{wm}^2 - (8\pi/g)(SOG)(T_{wm})\cos(\phi_w - COG+180°)\}^{0.5}], \qquad (2.5)$$

where g is the acceleration of gravity. Equation (2.5) was derived using the basic deep-water relationships between wavelength, wave period, and phase velocity. Because ϕ_w are only occasionally available from manual observations and are therefore poorly known, especially for different wave periods or wavelengths, and because much of the flux sampling from the *Knorr* was done while the ship was facing into the wind (and hence waves) and moved only very slowly forward, T_w was only computed for SOG < 2 m s^{-1} and ϕ_w was assumed to be the same as the wind direction. Errors in T_w are then less than 5% for all wave periods for ϕ_w within 35° of the wind direction and less than 2% for ϕ_w within 29° of the wind direction and T_w > 3.4 s. The ϕ_w of the longer-period waves are the most likely to differ from the wind direction (e.g., Rieder *et al.* 1994), and these differences are rarely greater than 60°, as shown in section 6. For differences of 60°, the maximum error in T_w for moderate or long periods (T_w > 6.4 s) is 6.1%.

Waves measured in this manner include both wind waves and swell, and only manually observed wave directions are available. The significant wave height (h_{sig}) is computed as four times the standard deviation of the surface-height time series (e.g., Neumann and Pierson 1966, pg. 351), and the significant wave period (T_{sig}) is the mean of the periods of the largest one-third waves. Wave-height power spectra were also computed using a fast-Fourier transform. The peaks of these spectra provided another estimate of the dominant wave period. Unpublished comparisons between the ship-mounted TSK wave-height sensor and wave buoys indicate agreement when significant wave heights are less than 4 m. For larger h_{sig}, some comparisons indicate that the TSK sensor overestimates the wave heights by 0.5-2 m (F. Dobson, private

communication; D. Stredulinsky, private communication) and others report that it underestimates them (J. Edson, private communication). However, these tests were done with the TSK-bearing ship moving at 5-8 m/s rather than nearly stationary as for the FASTEX sampling. The hour containing the three-minute sample shown in Fig. 2 had a mean wind speed of 20 m s^{-1}, a h_{sig} of 6.9 m, a T_{sig} of 8.7 s, and a maximum wave height (h_{max}) of 15.5 m. This maximum wave is seen at hour 11.278 in Fig. 2, and is embedded in waves with a large range of heights.

3. ENVIRONMENTAL DESCRIPTION

(a) Cruise track, sampling strategy, and general environment

The collection of the data used in this study began on December 23, 1996, southwest of the United Kingdom, and continued until January 27, 1997, when the R/V *Knorr* entered the port of Halifax, Nova Scotia (Fig. 3). The data "shake-down" portion of the cruise during December 22-27 took place in the southern end of the English Channel and southwest of Ireland. Sampling started on the main portion of the cruise on December 30 after leaving Cork, Ireland. Before January 20, the R/V *Knorr* was in the Gulf Stream waters south and east of the strong sea-surface temperature gradient ("SST wall") to the northwest. The area defined by (40-50° N, 30-40° W) in the central Atlantic was called the FASTEX near-upstream (NUS) domain. After January 20, the *Knorr* headed toward Halifax west of the Gulf Stream approximately along 45° N latitude, stopping to sample storms as they occurred. The SST gradient at the SST "wall" was actually about twice as strong as that depicted by the ECMWF analysis shown in Fig. 3, since the SST measured by the R/V *Knorr* on January 20-21 changed from 287.4 K to 275.8 K from longitude 43.9° W to 48.5° W while Fig. 3 indicates a SST change from 283.5 K to 278.5 K for this same track. Hence, near 45° N, the Gulf Stream SST "wall", bracketed by the vertical lines, is actually slightly farther west than suggested by the ECMWF analysis, and is better represented by the detailed fields given by Eymard *et al.* (1999).

Using weather forecasting material provided by the United Kingdom Meteorological Office and the FASTEX Operations center, the ship was positioned to sample the strongest winds available for a given storm, and to maintain an approximate north-south line with the other FASTEX ships between January 9-20. Generally, the *Knorr* was in the middle of the line. In order to maximize the amount of high-quality, high wind speed data collected, an effort was made to only move the ship during periods of weak winds and high pressure. During the stronger wind periods, the ship was turned into the wind (and usually the waves), and measurements were made while the ship moved forward 1-2 m s^{-1} relative to the water. This strategy was used throughout the cruise, even during the portion after leaving the NUS and heading toward Halifax.

Of the 15 storms and frontal waves sampled by the R/V *Knorr*, indicated by their pressure troughs and (usually) associated wind speed peaks in Fig. 4, seven were FASTEX intensive observation periods (IOPs) while the others occurred either before the field program started on January 9, or were storms forecast not to enter the FASTEX mesoscale sampling area near Ireland 18-48 h downwind of the R/V *Knorr*. During the "shake-down" portion of the cruise, post-frontal high pressure dominated with moderate-to-strong winds from the European continent.

(b) Atmospheric surface layer

Over 150 hours of flux data in wind speeds greater than 15 m s^{-1} (at 19-m height) were collected (Fig. 5), representing a significant increase in the direct covariance flux data collected under high wind speed, open-ocean conditions. Measurements were obtained in various stability regimes from within the cold air ahead of highly occluded fronts, below the low-level jet in the warm sector, and in the cold air behind cold fronts. In general, east of the Gulf Stream "wall," the sampled data were unstable with the air cooler than the sea surface. A few cases of weakly stable conditions were sampled. Over the cold waters west of the Gulf Stream wall the distribution was bimodal, with warm sector regimes providing mainly stable conditions and post-cold frontal regimes providing unstable environments. Significant numbers of hours with wind speeds between 15-22 m s^{-1} were sampled in all of these stability conditions. For hours for which τ_c, H_{sc}, and H_{lc} were all available, the stability parameter z/L as a function of wind speed can be calculated, where z is the wind measurement height (= 19.2 m), L is the Obukhov length defined by

$$L = (T u_*^2) / [\kappa g (t_* + 0.61 T q_*)] , \qquad (3.1)$$

and κ is the von Kármán constant (= 0.4). Plotting z/L as a function of wind speed shows that the environments for most wind speeds > 10 m s^{-1} were weakly unstable ($-0.1 < z/L < 0$) east of the Gulf Stream wall, while both weakly unstable and stable conditions occurred west of it (Fig. 6).

In general, the surface streamwise stress increases rapidly with wind speed with a modest scatter around this curve [Fig. 7(a)]. Hourly average stresses as much as 1.5 N m^{-2} were observed. Many of the surface flux parameterization schemes, including COARE 3.0, were developed from data with wind speeds below 12 m/s. This corresponds to a stress of about 0.3 N m^{-2}, or only 20% of the range observed in the FASTEX data set. During FASTEX, a slight positive average cross-stream stress was observed for all wind speeds [Fig. 7(b)], implying a mean stress from the right when facing upwind. This component averages less than 0.1 N m^{-2}, though individual points up to 0.5 N m^{-2} occur for wind speeds greater than 8 m s^{-1}, while the negative excursions are smaller but also tend to occur for the moderate to strong winds. This average positive cross-stream stress is believed to be physical and has significance when relating the surface stress to the synoptic environment, as will be discussed later.

Since the stability is near neutral in these high wind conditions, the errors in both the streamwise and cross-stream directions due to anemometer tilt errors should be fairly small. With observed boundary-layer depths of 500-1500 m (not shown) and a mast tilt in the along-ship (approximately streamwise) direction of 2° (see section 2.2b) and for stability of $-0.2 < z/L < 0$, the results of Wilczak *et al.* (2001 – see their Fig. 2) indicate that the error in the streamwise stress should be approximately 12-16%. The 1° mast tilt in the cross-ship (approximately cross-stream) direction suggests a cross-stream stress error of 6-8%.

The 10-m neutral drag coefficients (C_{Dn10}), sensible heat transfer coefficients (C_{hn10}), and moisture transfer coefficients (C_{en10}) are computed from both the covariance and inertial dissipation fluxes using the methods described by Fairall *et al.* (2003). As discussed by Fairall *et al.* (2003), for a neutral 10-m wind (U_{10n}) >12 m s^{-1}, the C_{Dn10} for the covariance technique is greater than that for the ID technique (Fig. 8a), and there is uncertainty as to which is correct.

The FASTEX C_{Dn10} from the ID technique are in good agreement with those from the ID technique of numerous other studies. The shaded area in Fig. 8a encompasses the ID curves

from Large and Pond (1982), Anderson (1993), Yelland *et al.* (1998), and Dupuis *et al.* (2003). It also encompasses the curves obtained from the buoy-based covariance measurements of Smith (1980), Large and Pond (1982), and Dupuis *et al.* (2003), the first two studies using the Bedford Institute buoy 10 km off the coast of Novia Scotia and the last study using the ASIS buoy 50 km from shore in the small, semi-circular Gulf of Lyon. Though only the long-fetch wind directions were used for these curves, it is unclear whether these coastal-zone measurements truly represent open ocean conditions, as the low-level airflow, the ocean wave conditions, and thereby the surface stresses are possibly affected by mesoscale atmospheric phenomena and wave reflections attributable to their coastal location. Only the measurements of Eymard *et al.* (1999) and Dobson *et al.* (1994) produced ID curves similar to the FASTEX covariance curves, though these ID estimates were not corrected for flow distortion, while nearly all those within the shaded area were. The flow distortion corrections will generally reduce the C_{Dn10} for a given U_{10n}, as shown by Dupuis *et al.* (2003).

Since this FASTEX data set represents the only ship-based, covariance flux measurements in an open-ocean, storm environment, and possibly the only covariance flux measurements in an open-ocean, storm environment regardless of platform (depending on the interpretation of the representativity of the coastal, buoy-based covariance flux measurements), it is difficult to ascribe a reason for the difference between the FASTEX covariance and ID C_{Dn10}. It is possible that flow distortion effects on the turbulent eddies have led to this difference, as the effect of flow distortion on the covariance flux measurements appears to be greater than for the ID technique (e.g., Edson *et al.* 1991), but the specific effects on turbulent eddies are unknown as are the specific effects on the turbulence at the sonic anemometer location of the R/V *Knorr*. However, the ID assumptions of an empirical imbalance term, a varying Kolmogorov "constant", and a zero pressure-term effect on the kinetic energy balance lead to errors, especially at higher wind speeds. Janssen (1999) showed that the perturbation-pressure term in the kinetic energy balance became significant at higher wind speeds and larger swell, thereby greatly increasing the C_{Dn10} estimates from the ID technique. Curve J99 in Fig. 8a shows that Janssen's pressure-term correction of the ID results from Yelland and Taylor (1996) produces C_{Dn10} slightly greater than the covariance values measured during FASTEX. Before correction, the ID results from Yelland and Taylor (1996) were located within the shaded area in Fig. 8a. Hence, while the agreement between the C_{Dn10} from the flow-distortion corrected ID technique and the buoy-based covariance measurements suggests that the FASTEX ship-based covariance fluxes may be too large, possibly due to unknown effects of flow distortion, the assumptions in the ID technique at high winds as represented by the Janssen (1999) study suggests that the FASTEX covariance fluxes may be closer to the truth than the ID fluxes, implying that the buoy-based covariance flux measurements may have been affected by coastal effects. As a further complication, the Janssen (1999) results are also a contentious issue and a source of scientific debate (Taylor and Yelland 2001a; Janssen 2001).

Until the above issues are resolved, we feel that the current best estimate of the C_{Dn10} from the FASTEX data is represented by the average of the two methods. The linear fits to the average curves are represented by the heavy dashed lines in each panel of Fig. 8 and are given by

$$C_{Dn10} = (0.0768 \times U_{10n} + 0.603) \times 10^{-3} \qquad 6 \text{ m s}^{-1} < U_{10n} < 19 \text{ m s}^{-1}, \; r^2 = 0.92, \qquad (3.2a)$$

$$C_{hn10} = (0.0298 \times U_{10n} + 0.922) \times 10^{-3} \qquad 6 \text{ m s}^{-1} < U_{10n} < 19 \text{ m s}^{-1}, \; r^2 = 0.58 \qquad (3.2b)$$

$$C_{en10} = (-0.0011 \times U_{10n} + 1.297) \times 10^{-3} \qquad 6 \text{ m s}^{-1} < U_{10n} < 18 \text{ m s}^{-1}, \; r^2 = 0.01, \qquad (3.2c)$$

where r^2 is the correlation coefficient of the regression to the bin averages.

The surface flux scheme of Fairall *et al.* (2003) predicts C_{Dn10} between the two observed FASTEX curves close to the average. The *Knorr* data suggest a slight increase in C_{hn10} with U_{10n}, though the scatter around the mean values gives us only low confidence in this trend. Note that the H_{sc} used in the calculation of the C_{hn10} are corrected for a bias as described in section 2.2b. If uncorrected H_{sc} were used, the slope of (3.2b) is only slightly larger. The C_{en10} from the *Knorr* is essentially constant near 1.3×10^{-3}, slightly higher than that predicted by the model of Fairall *et al.* (2003).

(c) Ocean surface characteristics

The atmospheric surface layers sampled by the R/V *Knorr* during FASTEX were either over the relatively warm waters of the mid-Atlantic Gulf Stream east of the Gulf Stream "wall," or in the much colder waters of the Labrador current west of the Gulf Stream. In the former area, the observed SSTs were 11-18°C, while in the latter they were 2-6°C, producing different stability distributions in each region (see Figs. 3, 5, and 6).

During the cruise, the significant wave height was approximately constant at 4 m for wind speeds less than 10 m s^{-1}, and generally increased with increasing wind speed for speeds above, reaching values of about 6.5 m for a 22 m s^{-1} wind (Fig. 9a). However, there is a large scatter around this mean curve. The 4-m wave heights for the lower wind speeds represent the constant swell conditions in the mid-Atlantic Ocean. The maximum wave heights averaged nearly 12 m for winds near 20 m s^{-1}, but the maximum wave heights are widely scattered around the bin-averaged curve, including one of 14.5 m for a 10 m s^{-1} wind speed. A maximum wave height of 15.7 m occurred for a wind of 19.3 m s^{-1} on January 4. One nearly as high (15.5 m) is shown in Fig. 2. Neither of these hours is included in Fig. 9a, as covariance stresses weren't obtained for these hours. The mean period of the significant waves was approximately 8.2-8.7 s for weak winds, had a minimum of about 7.5 s for 10-11 m s^{-1} winds, and slowly increased to 9.2 s for 22 m s^{-1} winds (Fig. 9b). Estimates of the significant wave heights and periods of waves in equilibrium with the local winds show that the waves were rarely in equilibrium with the local winds. Hence, equilibrium relationships are not useful for describing the wave characteristics in the FASTEX environment. In particular, the equilibrium characteristics underestimate the significant wave heights at weak winds since there is nearly always a significant swell. For the strongest winds, the equilibrium characteristics are closer to the characteristics of the tallest waves rather than the significant waves, suggesting that the atmospheric conditions producing the strong winds are too transient to allow the local waves to reach equilibrium. The equilibrium wave conditions were calculated by the relationships in the appendix of Taylor and Yelland (2001b).

The relationship between the wave characteristics and the measured surface stress is not strong in the data. There is an indication that the surface stress increases with significant wave height [Fig. 10(a)], though the scatter of the hourly values around this curve is significantly greater than the scatter around the curve for the stress as a function of wind speed in Fig. 7(a). The relationship between the mean period of the significant waves and the surface stress is even more complex [Fig. 10(b)]. In addition, there appears to be no obvious relationship between the wave characteristics and the cross-stream stress (not shown).

4. COMPOSITING METHOD

In this and the next two sections, we will show that the surface-layer and ocean characteristics that showed a large scatter in the traditional presentations in section 3 have clear relationships to the synoptic environment. In order to place the observations in a storm-relative framework, the start of the warm sector (WSB), the surface cold-frontal passage (CFP), and the end of the post-frontal baroclinic regime (PFE) were defined from basic meteorological parameters. The near-surface specific humidity was used as a key parameter to define the WSB and the PFE. The surface increase of specific humidity at the WSB and the disappearance of the humidity perturbation at the end of the PFE were clear in every case [e.g., Fig. 11(a)]. The CFP was defined by the surface wind-direction shift [Fig. 11(a)]. Therefore, the warm sector region is defined as the time between the increase in the surface specific humidity and the wind-direction shift, while the post-frontal baroclinic zone regime is defined as the period between the wind-direction shift and the end of the decrease in specific humidity. Typical changes in air temperature, wind speed, surface pressure, and precipitation were often seen [e.g., Figs. 11(b), (c), and (d)], though these weren't used to define the transitions. Note that in Fig. 11 (and Fig. 16), the time increases from right to left along the abscissa in order that the warm sector and post-frontal air have the same spatial relationship to the cold front as when observing a storm system from a satellite image (e.g., Fig.12).

With these definitions, statistical composites of storm-relative atmospheric parameters, surface fluxes, and wave characteristics were computed for the R/V *Knorr*. The composites were temporally normalized using the duration of the warm sector region for each case. Again, the abscissae of the composites are defined so the normalized time ($\tilde{t}$) increases with real time and the warm sector is to the right and the post-frontal air is to the left of the cold front. Hence the warm sector occurs for a $\tilde{t}$ from -1 to 0 and the post-frontal region occurs for $\tilde{t}$ from 0 to 1 (though the post-frontal region in most cases extended only from 0 to ~ 0.5). The difference in duration between the post-frontal region and the warm sector led to fewer samples during the latter half of the normalized post-frontal region.

Mathematically, the compositing can be expressed as

$$\tilde{\lambda}_k'(i) = \langle \lambda_j(i) - \lambda_{wsb}(i) \rangle, \tag{4.1}$$

$$\tilde{d}_k'(i) = \langle d_j(i) - d_{cfp\text{-}1h}(i) \rangle, \tag{4.2}$$

$$\tilde{\alpha}_k(i) = \langle \alpha_j(i) \rangle, \tag{4.3}$$

where λ represents air temperature (t_a), specific humidity (q_a), and wind speed (ws); d is the wind direction; α represents all other composited variables such as τ_c, τ_{ID}, τ_b, H_{sc}, H_{sID}, H_{sb}, H_{lc}, H_{lID}, H_{lb}, h_{sig}, h_{max}; the $\langle\ \rangle$ indicates averaging over the observation times t_j that produce normalized times, $\tilde{t}_j$, within the k^{th} normalized time interval of length 0.1 through

$$\tilde{t}_j(i) = [t_j(i) - t_{cfp}(i)]/[t_{cfp}(i) - t_{wsb}(i)], \tag{4.4}$$

i is the index for each frontal case, and the prime represents a storm-perturbation quantity. For each normalized time interval k, the mean of each variable over the 10 cases (for i = 1:10) are

computed. For various reasons, some $\tilde{t}_k$ for some variables have fewer than 10 cases. The temporal normalization (4.4) removes biases resulting from the physical size and translation speed of the storm. By first obtaining average values for each normalized time and each storm and then averaging the ten storms gives equal weight to each synoptic case, regardless of the number of measurements for each case.

The storms' movements past the *Knorr* and the other FASTEX research vessels produced a northeast-to-southwest time-to-space adjusted "track" for each ship through each storm (Fig. 12). The orientation and path of the storm determined the obliqueness of the ships' tracks relative to the frontal cloud bands. For example, the tracks were nearly orthogonal to the surface cold front in cases 3 and 6, while they were nearly parallel for cases 4 and 8. Since the R/V *Knorr* had to pass through the warm sector of an open frontal wave in order that the data be useable in this compositing method, only 10 out of the 15 cases shown in Fig. 4 are used, and these cases are listed in Table 2. The duration of the warm sector averaged 17.7 hours, ranging from 3.1-43.4 hours. The post-frontal region was less than half that in duration. Because $\tilde{t}$ is defined using the duration of the warm sector region, most cases have no data beyond $\tilde{t} = 0.5$. The first seven cases were obtained south and east of the Gulf Stream SST "wall," while the last three cases were obtained in the colder waters to the north and west.

While normalizing with the duration of the warm sector is appropriate for studying the warm sector, a normalization of the post-frontal region is probably better done using the duration of the post-frontal period, though this would lead to a change in time scales at the cold front. Though not shown, such a scaling has also been done, and the results are similar to those to be shown using the warm-sector time scaling for the entire storm period except that data extends to $\tilde{t} = 1$.

Synoptic storm systems provide the principal source of variability in low-level, extratropical, atmospheric structure. Furthermore, numerous studies show repeatable mesoscale structure at low levels in the warm sector and near cold fronts of oceanic midlatitude storms, such as a plume of higher specific humidity, warmer temperatures, and a low-level jet (LLJ) (e.g., Browning and Pardoe 1973; Hobbs *et al.* 1980; Wernli 1997; Ralph *et al.* 2004). Since these features are generally dynamically linked, we expect that the composites will show systematic changes in the principal atmospheric parameters. Because, in a bulk sense, the surface fluxes are related to the principal atmospheric parameters, we also expect that the flux composites will show systematic changes in the surface-layer fluxes relative to the storm systems. Departures from this systematic behavior of the fluxes will indicate the effects of other processes, such as changes in the surface wave characteristics and sea-surface temperature.

5. COMPOSITE SURFACE LAYER

(a) Atmospheric

The composites of the basic surface-layer parameters of air temperature, specific humidity, wind speed, and wind direction show regular variations relative to the location of the surface front (Fig. 13). The air temperature shows an increase of about 4°C from the WSB ($\tilde{t} = -1$) to just before the CFP ($\tilde{t} = 0$), decreasing behind the cold front. The specific humidity increases nearly 4 g kg^{-1} within the warm sector, peaking just before the CFP. The wind speed shows the surface-layer manifestation of the classical low-level jet (LLJ) shortly before the

frontal passage, with an increase of about 8.5 m s^{-1} from the WSB. The maximum composite wind speed (not shown) was about 17 m s^{-1} in the warm sector, though the maximum 15-min 19-m wind speeds during the warm sector averaged 19.7 m s^{-1}, and ranged from 18-22 m s^{-1} (Table 2). The wind speed initially drops at the CFP, but then increases to another peak in the post-frontal region. An examination of associated satellite images showed no obvious post-frontal circulation or frontal features, suggesting that this post-frontal peak is most likely due to enhanced vertical mixing because of the weaker post-frontal stability. In the transition from the eastern edge of the warm sector, the wind direction initially has a more westerly component than at the CFP, and then a slightly more easterly component. This implies that the surface-layer flow is diffluent at the eastern edge of the warm sector, and then becomes slightly confluent near the middle of the warm sector to just before the cold frontal passage. Note that the onset of the wind speed increase occurs west of the eastern edge of the warm sector (near $\tilde{t} = -0.9$) as defined by the specific humidity. Hence, the thermodynamic and kinematic definitions of the warm sector region aren't exactly coincident. The main storm-generated variations are qualitatively present in all cases, as indicated by the hourly standard deviations that are smaller than the amplitudes of the storm-generated variations.

Though the wind direction changes by 100° after the CFP, the ship-relative wind direction (not shown) changes only by about 5° since the orientation of the ship was adjusted as the wind shifted. This minimizes directional differences of flow distortion effects when examining the flux changes between the warm sector and post-frontal sector.

(b) Oceanic

The significant wave heights increased from about 3.5 m in the eastern half of the warm sector to about 5.3 m at the time of frontal passage [Fig. 14(a)] and in the post-frontal region. The maximum wave heights (h_{max}) were about 5.5 m in the eastern half of the warm sector, increasing to about 9 m at the time of frontal passage. The ratio h_{max}/h_{sig} abruptly increased from about 1.5 in the eastern part of the warm sector region to about 1.75 during the time bracketing the cold-frontal passage. The period of the significant waves was at a minimum of 7.5 s in the middle of the warm sector, and reached a maximum of 8.3 s at the cold frontal passage and 8.5 s just east of the warm sector [Fig. 14(b)]. Hence, wave growth and an increase of the wave period occur in the western half of the warm sector, and a systematic physical mechanism, perhaps due to a combination of the changing swell and wind directions in the vicinity of the front, causes occasionally taller waves.. Note that the changes in wave height and period don't occur until after the onset of the increase in the wind speed at $\tilde{t} = -0.9$.

Since high-frequency (small period) waves tend to respond more quickly to changes in the wind than low-frequency (large period) waves (e.g., Rieder and Smith 1998), we find it useful to split the wave data into wave period bins of less than 3.4 s, 3.4-6.4 s, 6.4-9.5 s, and greater than 9.5 s. Using deep water gravity wave relationships, these period bins correspond to wavelength bins of < 18 m, 18-64 m, 64-141 m, and > 141 m, respectively. We find the following: 1) the frequency of the waves with relatively short 3.4-6.4 s periods peaks in the eastern one-half of the warm sector as the wind speed begins to increase, and then decreases (Fig. 14c); 2) the frequency of occurrence of waves with periods > 6.4 s increases in the western two-thirds of the warm sector at the expense of the waves with periods < 6.4 s [Fig. 14(c)]; 3) the mean height of the waves with periods >3.4 s increases in the warm sector [Fig. 14(d)]; and 4) the onset of the height increase and the peak in height occurs earlier (later) for the shorter

(longer) period waves than for the ones with longer (shorter) periods. The longest period waves have their maximum wave height in the post-frontal regime or east of the warm sector. These composite wave period changes are consistent with the case shown by Rieder and Smith (1998).

6. COMPOSITE SURFACE FLUXES

Turbulent fluxes were determined through the covariance technique, the inertial dissipation technique, and the bulk formulas of Fairall *et al.* (1996, 2003). The covariance values show the increase of stress beginning at $\tilde{t} \approx -0.75$ [Fig. 15(a)], shortly after the time the wind speed increases [Fig. 13(c)] and at the time the wave characteristics respond (Fig. 14). A peak stress of 0.7 N m^{-2} occurs shortly before the cold frontal passage at the time of maximum surface-layer wind speed, peak in the occurrence of the 6.4-9.5 s period waves and near the peak in heights of these waves. Comparably high, or even slightly higher, values of stress occur in the post-frontal regime, roughly corresponding to the secondary wind-speed maximum and the end of the change in wind direction.

The covariance sensible heat flux (H_{sc}) is a maximum in the post-frontal regime and before the onset of the warm sector [Fig. 15(b)]. Within the warm sector, H_{sc} decreases slowly as the front approaches the ship, becoming slightly negative just before the passage of the surface cold front. Qualitatively, this is consistent with the warming of the prefrontal air through horizontal advection and surface-layer fluxes producing a stable environment nearest the front and hence negative H_s (e.g., Bond and Fleagle 1988). The latent heat flux (H_{lc}) also decreases within the warm sector [Fig. 15(c)] as the specific humidity increases [Fig. 13(b)]. However, the specific humidity does not increase sufficiently to produce a negative H_{lc}. Hence, in contrast to H_{sc}, H_{lc} remains positive. The maximum H_{lc} occurs just before the onset of the warm sector and at the very end of the post-frontal regime.

The streamwise and cross-stream covariance stress components can be combined to compute a stress direction. If the stress is due entirely to wind waves, then the stress direction should be the same as the wind direction. However, previous observations have noted that the stress and wind directions often are not the same, and that these directional differences may be due to the effects of swell (Geernaert *et al.* 1993; Grachev *et al.* 2003) or baroclinicity (Geernaert 1996). The composite of the difference between the stress and wind directions [Fig. 15(d)] shows that in the central and western portion of the warm sector, the stress direction is often greater than the wind direction by 5-12° (that is, the stress direction is to the right of the wind direction), while in the post-frontal regime the directional difference is of the same magnitude but with opposite sign.

If swell is influencing the stress, then the stress direction should be between the swell and wind directions (Grachev *et al.* 2003). Manual observations of the swell direction by the ship's crew on the bridge of the R/V *Knorr* show that the warm sector stress direction is frequently between the swell direction and the wind direction. Figure 16 shows an example where the difference between the wind direction and swell direction occurs mainly in the two warm sectors. Hence, since the stress vector is influenced by the swell direction, the difference between the wind direction and stress direction occurs only in the warm sector for these two cases. The post-frontal regime differences shown in Fig. 15(d) are produced by other cases. Apparently, in some cases, the pre-frontal swell direction can be influenced by the post-frontal swell direction, probably through different phase velocities of the swell and the cold front. Therefore, the swell direction appears to change before the wind direction near 7.5-7.8 in Fig. 16. These results

suggest that in the vicinity of fronts, the stress vector may not be an accurate indicator of the wind direction, either in the warm sector, post-frontal regime, or both.

Inertial dissipation (ID) calculations of the surface fluxes (Fig. 17) also show the same qualitative trends that were noted for the covariance fluxes (Fig. 15). However, the ID stresses are slightly smaller than the covariance stresses, especially in the higher wind-speed regime in the vicinity of the fronts. Furthermore, the ID sensible heat fluxes are lower near the fronts and higher in other areas. The differences in H_l are not quite as systematic, though there is still a tendency for the ID H_l to be weaker in the vicinity of the front and stronger in the eastern half of the warm sector. These differences may reflect either flow distortion or ship-motion problems for the covariance technique at high wind speeds, or the inapplicability of the assumed inertial subrange characteristics at these wind speeds and/or environmental conditions (e.g., see discussion in section 3b or in the Appendix of Fairall *et al.* 2003).

The bulk fluxes [Fig. 18(a)-Fig. 18(c)] calculated from the measured basic parameters and the bulk relationships of Fairall *et al.* (1996, 2003) show the same general characteristics as discussed for the covariance and ID fluxes. However, the differences plot [Fig. 18(d)] shows that the bulk stresses are substantially (up to 0.25 Nm^{-2}) smaller than the covariance estimates, particularly in the post-frontal regime. Large and Pond (1981) attributed such a discrepancy in stress to the rougher seas after a front due to the change in wind direction, a phenomenon not included in parameterization schemes. Note that the maximum in $\tau_{sc} - \tau_b$ does occur during the period of greatest wind direction change [compare with Fig. 13(d)]. The secondary peak in stress error in the warm sector of about 0.1 N m^{-2} suggests that the parameterization scheme also does not increase the stress sufficiently as the wind speed increases. The bulk H_s are within 20 W m^{-2} of the covariance estimates. The bulk H_l appear to be 40-60 W m^{-2} larger in most of the warm sector and 20-40 W m^{-2} smaller in portions of the post-frontal regime. The reasons for the differences between the covariance, inertial dissipation, and the bulk fluxes may include flow distortion effects on turbulent eddies, errors due to the assumptions inherent in the inertial dissipation and bulk techniques, and real effects of the wind and wave conditions in the vicinity of the fronts.

7. DISCUSSION

While previous investigations have examined the contribution of synoptic variability to variations in surface fluxes for individual storms, to our knowledge, this is the first attempt at compositing the fluxes from multiple storms. Such compositing allows us to make broader conclusions regarding the relationships between the surface fluxes and the synoptic environment than would be possible from only a single case study. In studies of maritime storm systems, the synoptically forced variations of the near-surface atmospheric parameters are frequently considered to be damped compared to their land-based counterparts, primarily through the effects of surface fluxes. The variations in the composites for the surface-layer atmospheric parameters (Fig. 13) permit us to quantify these synoptically forced variations for the North Atlantic Ocean, showing that changes of 4-5°C in temperature, 3.5-4 g kg^{-1}in absolute moisture, and 8-12 m s^{-1} in near-surface wind speed are typical variations associated with atmospheric cold fronts over the open ocean. Similar compositing studies can and should be done using a longer database of buoy and ship data to obtain more statistically significant variations than can be obtained with this 5-week data set.

This compositing method also allows us to obtain insights into the synoptically modulated physical processes producing the observed surface fluxes. The variations of the surface sensible and latent heat fluxes indicate that they are primarily determined by the synoptically-driven, low-level, thermal and moisture advection. While relatively dry and cool air exists outside the warm-sector region of the cyclones, the strong southerly flow within the warm sector, maximizing near the surface cold front, advects warmer and moister air northward. This advected air is typically warmer than the local SST, hence producing a small downward sensible heat flux. Upward sensible heat flux may contribute to warming the air in the slightly cooler eastern portion of the warm sector [e.g., Fig. 15(b)], which can then contribute to the warm air advection as the confluent southerly flow brings this air closer to the front further north. Generally, the specific humidity of the warm sector air, even closest to the front, is not as large as the saturated specific humidity given by the local SST, leading to a positive latent heat flux in the warm sector of 30-140 Wm^{-2}, which contributes significant moisture to the strong southerly flow. Both the sensible and latent heat fluxes are significantly larger in the post-frontal region where the advected air is cooler and drier, but they may be dynamically less important in this region.

The strong southerly winds near the cold front in the warm sector and the even stronger west-northwesterly winds in the post-frontal regime lead to peaks in the surface stress [Figs. 13(c) and 15(a)]. The significant wave heights reach a maximum just before the passage of the cold front and remain high throughout the post-frontal period, while the waves before the warm sector and near the cold-frontal passage have the longest periods [Fig. 14(a) and Fig. 14(b)]. The wave conditions likely contribute to the variations in stress, since, for instance, the bulk estimate of the stress, which does not explicitly account for variations in wave height or period, significantly underestimates the stress in the middle of the warm sector [when waves are growing and the frequency of waves with intermediate periods peaks – Fig. 14(c)] and in the first portion of the post-frontal region (when the wind direction is changing) [Fig. 18(d)].

Systematic differences between the wind direction and stress direction occur and change sign from the warm sector to the post-frontal regions [Fig. 15(d)]. One possible explanation is that stress effects from swells are present (Geernaert *et al.* 1993; Rieder *et al.* 1994; Grachev *et al.* 2003) and that swell orientations change much less or more slowly across a cold front than does wind direction, as shown in Fig. 16. Physically, this may result either because the swells move faster than the cold front so post-frontal swell orientations are found ahead of the cold front, or because a cold front moves fast enough to not influence the swells over a long enough time period to change their orientation to that of the winds. Geernaert (1996) has also suggested that the thermal wind effects can reorient the turbulent eddies, so the stress direction differs from the wind direction when significant thermal gradients in the low-level along-wind direction are present. Since strong along-wind thermal gradients are generally present within the warm sector and in the post-frontal regime, and the thermal wind will generally change less rapidly than the surface wind across a front accounting for the change in sign of the stress-wind dircetional differences, this mechanism is also plausible from our data set. However, application of Geernaert's eq. 12 produces angular differences between the stress and wind direction that are 3-4 times larger than observed, while the limited swell directional data such as in Fig. 16 show that the stress direction is between the swell and wind directions, supporting the first hypothesis. Though these FASTEX observations show the presence of these stress-wind directional differences and show that they do occur in frontal regions of large thermal gradients and significant changes in wind direction, our data does not show conclusive evidence supporting

one mechanism or the other. Additional studies directly linking the swell to the stress are needed for this. Furthermore, the presence of these directional differences implies that satellite-based scatterometer wind directions, which rely on the surface stress field, will be in error and will underestimate the surface directional wind shift across the front and thus the derivative fields, such as convergence and vorticity. However, if such directional biases are seen in the scatterometer comparisons with other wind measurements, their magnitude is such that they may be ascribed to uncertainties in the observations.

The compositing of the FASTEX data also provides suggestions of possible influences of the surface fluxes on the maritime synoptic evolution in this region, which was an important objective of FASTEX. In an adjoint modeling study, Langland *et al.* (1995) show that the development of maritime cyclones are sensitive to the surface heat fluxes in the warm sector regions. Other studies of the influence of surface sensible and latent heat fluxes on the development of maritime extratropical cyclones have shown that when heat fluxes are negative within the warm sector ahead of a cold front and positive in the post-frontal region, such a configuration does not promote development of the surface low (e.g., Haltiner 1967; Kuo *et al.* 1991) and may even be slightly detrimental to its development (e.g., Reed and Simmons 1991). However, when the surface heat fluxes are positive in the warm sector region, especially during the earlier portions of the cyclone development, they contribute significantly to the cyclogenesis through decreased stability and increased moisture content and subsequent latent heating (e.g., Kuo *et al.* 1991; Zhang *et al.* 1999; Gyakum and Danielson 2000). Our study shows that the composite sensible heat fluxes in the warm sector region are near zero or slightly negative in these 10 FASTEX storms, but that the composite latent heat flux is positive. Hence, the composite sum of the surface heat fluxes in the warm sector is positive and we can conclude that the warm sector surface heat fluxes, dominated by the latent heat flux, in these FASTEX storms should contribute to the development of the associated cyclones.

The observed variation of the surface stress also has implications for the dynamical feedback to the cyclone development. Low-level maxima of dry potential vorticity (PV_d) along the cold front have been hypothesized to lead to the development of frontal waves and frontal cyclones (Joly and Thorpe 1990). These low-level PV_d maxima are believed to be produced by diabatic processes, especially latent heating in the main updraft near the surface cold front (e.g., Persson 1995, Stoelinga 1996). However, PV_d can also be modified by surface diabatic and frictional processes. Examination of the conservation equation for PV_d shows that the observed increase in the surface sensible heat flux toward the east in the warm sector would likely contribute to an increase in PV_d while the observed decrease in stress toward the east in the warm sector would likely contribute to a decrease. More quantitative analysis of the vertical gradients in addition to the horizontal gradients is necessary to determine which term would dominate, and is beyond the scope of this paper.

8. CONCLUSIONS

Surface layer and flux data were collected during FASTEX from the R/V *Knorr* in high wind-speed conditions in the North Atlantic during December 1996 and January 1997. This data set includes the surface momentum, sensible heat and moisture fluxes calculated from three different methods, sea-surface temperatures, and wave characteristics, which were all used in this study. It is the only field experiment where ship-based, covariance flux measurements in an open-ocean storm environment have been successfully obtained. The data set also includes remote sensor and sounding data to be used in future studies. These measurements contribute

significantly to the limited set of surface flux measurements available from high wind environments, with 88, 77, and 44 hours of high-quality covariance momentum, sensible heat, and latent heat flux measurements, respectively, obtained for 10-m neutral winds in the 15-21 m s^{-1} range. The coincident measurement of wave heights through a microwave Doppler radar mounted in the bow of the ship adds additional value to this data set.

The 10-m neutral drag coefficients determined from the covariance technique are generally larger than those determined from the inertial dissipation technique. It is unclear whether this difference indicates the presence of flow distortion problems in the covariance data, or a failure of the assumptions inherent to the inertial dissipation technique at these higher winds. The inertial dissipation drag coefficients from the R/V *Knorr* during FASTEX are consistent with the limited inertial dissipation data from other measurements in open ocean storm environments. No other data sets of covariance measurements in such an environment are available for comparison. This data set also suggests that the 10-m neutral transfer coefficient for sensible heat flux increases slightly at the higher wind speeds. The linear best-fit lines for all of the transfer coefficients are given by equations (3.2a-c).

In order to illustrate the relationship between the surface layer and the synoptic atmospheric environment, composites of atmospheric surface layer measurements and ocean surface characteristics were computed along ship paths through 10 storms for which the *Knorr* passed through the open-wave warm sector and the cold front. These composites, summarized in Fig. 19, show the following:

a) The moistening and warming [Fig. 19(a)] associated with synoptic-scale advective patterns and surface-layer fluxes lead to minima in the sensible and latent heat fluxes just before the frontal passage [Fig. 19(b)], despite the strong surface winds at this time. Though the warm-sector sensible heat flux minimum is slightly negative, the sum of the two heat fluxes is positive, suggesting a positive impact on the synoptic development of these systems.

b) The momentum flux is a maximum just before the frontal passage during the peak in wind speed associated with the warm-sector low-level jet [Fig. 19(a) and Fig. 19(b)]. A second stress maximum of comparable magnitude occurs in the middle of the post-frontal regime. The patterns of heat and momentum fluxes should affect the surface potential vorticity generation, and have dynamical implications for the stability of the frontal zone for frontal wave development.

c) Wave heights increase steadily from the eastern half of the warm sector to the frontal passage, remaining high through most of the post-frontal regime before decreasing [Fig. 19(b)].

d) Differences between covariance and ID stresses are largest during the times bracketing the cold front when the wave heights and covariance stresses are large. Differences between covariance and bulk stresses are greatest in the pre-frontal low-level jet when the frequency of waves with intermediate periods of 6-9 s maximizes and in the post-frontal regime where wind direction veers.

e) The stress direction is consistently 5-12° to the right of the wind direction in the western half of the warm sector and 2-15° degrees to the left of the wind direction in the post-frontal regime, supporting previous observations [Fig. 19(b)]. The data suggest that these differences are due to influences of swell orientations, but can not exclude effects from thermal advection on the turbulent eddy orientation. Their presence implies possible errors in satellite-based scatterometer measurements of surface wind fields.

The FASTEX data set has already been used for validation of the performance of surface flux parameterization schemes (Brunke *et al.* 2003; Fairall *et al.* 2003). Planned studies will

utilize synoptic compositing of the atmospheric boundary-layer measurements to show how the synoptic environment modulates the boundary-layer structure and processes. Additional studies are required to examine the perplexing problem of how the surface waves influence the surface roughness in conditions of strong winds and swell, and how best to parameterize this effect for surface flux computations. Finally, the FASTEX data set from the R/V *Knorr* is useful as validation data for simulations of the FASTEX storm environments, with a focus especially on the impact of the surface fluxes and ocean characteristics on storm structure and development. The results of this current study give background and context to future studies.

ACKNOWLEDGEMENTS

The dedication and hard work by David Costa, Martin Mulhern, Serhad Atatürk, Gordon Maclean, and Louis Verstraete in collecting the data on the R/V *Knorr* in a difficult and sometimes dangerous environment are greatly appreciated. The professional and understanding support by the captain and crew of the R/V *Knorr* was crucial for the success of obtaining these measurements in difficult environmental conditions. Dr. Fred Dobson provided the TSK wave-height instrument and useful discussions regarding data processing and interpretation. Discussions with Dr. Andrey Grachev provided useful insights for interpretation of the stress direction results, and Paul Neiman provided excellent suggestions on an earlier manuscript. The deployment of the scientific equipment and data collection on the R/V *Knorr* was funded by NOAA/OAR director's discretionary funds. The data analysis was supported by NSF Grant ATM-9727054, with additional analysis support provided by NASA grant NAG5-10790.

REFERENCES

Anctil, F., Donelan, M.A., Drennan, W.M., and Graber, H.C. 1994 Eddy correlation measurements of air-sea fluxes from a Discus buoy. *J. Atmos. Ocean. Technol.* **11**, 1144-1150.

Anderson, R. J. 1993 A study of wind stress and heat flux over the open ocean by the inertial-dissipation method. *J. Phys. Oceanogr.*, **23**, 2153-2161.

Beljaars, A. C. M. 1995 The parameterization of surface fluxes in large scale models under free convection. *Q. J. R. Meteorol. Soc.*, **121**, 255-270.

Bond, N. A., and Fleagle, R. G. 1988 Prefrontal and postfrontal boundary layer processes over the ocean, *Mon. Weather Rev*., **116**, 1257-1273.

Browning, K.A., and Pardoe, C.W. 1973 Structure of low-level jet stream ahead of mid-latitude cold fronts. *Q. J. R. Meteorol. Soc.*, **99**, 619-638.

Brunke, M.A., Fairall, C.W., Zeng, X., Eymard, L., and Curry, J. A 2003 Which bulk aerodynamic algorithms are least problematic in computing ocean surface turbulent fluxes? *J. Clim*., **16**, 619-635.

Chertock, B., Fairall, C. W., and White, A. B. 1993 Surface-based measurements and satellite retrievals of broken cloud properties in the equatorial Pacific. *J. Geophys. Res*., **98**, 18,489-18,500.

Dobson, F. W., Smith, S. D., and Anderson, R. J. 1994 Measuring the relationship between wind stress and sea state in the open ocean in the presence of swell. *Atmos.-Ocean*, **32** (1), 237-256.

Dupuis, H., Guerin, C., Hauser, D., Weill, A., Nacass, P., Drennan, W. M., Cloché, and Graber, H. C. 2003 Impact of flow distortion corrections on turbulent fluxes estimated by the inertial dissipation method during the FETCH experiment on R/V *L'Atalante*. *J. Geophys. Res.*, **108,** C3, 8064, doi:10.1029/2001JC001075.

Dupuis, H., Taylor, P. K., Weill, A. and Katsaros, K. B. 1997 The inertial dissipation method applied to derive momentum fluxes over the ocean during the SOFIA /ASTEX and SEMAPHORE experiments with low to moderate wind speeds. *J. Geophys. Res.*, **102,** C9, 21115-21129.

Edson, J. B., Fairall, C. W., Mestayer, P. G., and Larsen, S. E. 1991 A study of the inertial-dissipation method for computing air-sea fluxes. *J. Geophys. Res*., **96** (C6), 10689-10711.

Edson, J.B., A. A. Hinton, Prada, K. E., Hare, J.E., and Fairall, C. W. 1998 Direct covariance flux estimates from moving platforms at sea. *J. Atmos. Ocean. Technol.*, **15**, 547-562.

Eymard, L., Caniaux, G., Dupuis, H., Prieur, L., Giordani, H., Troadec, R., Bessemoulin, P., Lachaud, G., Bouhours, G., Bourras, D., Guerin, C., Le Borgne, P., Brisson, A., and Marsouin, A. 1999 Surface fluxes in the North Atlantic current during CATCH/FASTEX. *Q. J. R. Meteorol. Soc*., **125**, 3563-3599.

Fairall, C. W., and Larsen, S. E. 1986 Inertial dissipation methods and fluxes at the air-ocean interface. *Bound.-Layer Meteorol*., **34**, 287-301.

Fairall, C. W., and Young, G. S. 1991 A field evaluation of shipboard performance of an infrared hygrometer. *Proc., 6th AMS Symp. for Meteorological Observations and Instrumentation*, June 12-16, New Orleans LA, 311-315.

Fairall, C. W., Bradley, E. F., Rogers, D.P., Edson, J.B., and Young, G.S. 1996 Bulk parameterization of air-sea fluxes for TOGA-COARE. *J. Geophys. Res.*, **101**, 3747-3764.

Fairall, C. W., White, A. B., Edson, B., and Hare, J. E. 1997 Integrated shipboard measurements of the marine J. boundary layer: *J. Atmos. Ocean. Technol.*, **14**, 338-359.

Fairall, C. W., Persson, P. O. G., Bradley, E.F., Payne, R.E., and Anderson, S.A. 1998 A new look at calibration and use of Eppley precision infrared radiometers Part I: Theory and application. *J. Atmos. Ocean. Technol*., **15**, 1230-1243.

Fairall, C. W., Hare, J. E., Grachev, A. A., and White, A. B. 2000 Preliminary surface energy budget measurements from Nauru '99. *Proc. 10th ARM Science Team Meeting*, San Antonio, TX, http://www.arm.gov/docs/documents/technical/conf_0003/fairall(1)-cw.pdf

Fairall, C. W., Bradley, E. F., Hare, J. E., Grachev, A., and Edson, J. B. 2003 Bulk parameterization of air-sea fluxes: Updates and verification for the COARE algorithm. *J. Clim*., 16, 571-591.

Geernaert, G. L., Hansen, F., Courtney, M., and Herbers, T.	1993	Directional attributes of the ocean surface wind stress vector. *J. Geophys. Res.*, **98**, 16,571-16,582.
Geernaert, G. L.	1996	On modeling the wind stress direction based on thermal advection and surface waves. *Proceedings, Symp. on the Air-Sea Interface, Radio and Acoustic Sensing, Turbulence and Wave Dynamics*, 24-30 June, 1993, M. A. Donelan, W. H. Hui, and W. J. Plant, eds. Marseilles, 421-427. [Available from The Rosenstiel School of Marine and Atmospheric Science, University of Miami, 4600 Rickenbacker Causeway, Miami, FL 33149-1098, USA]
Grachev, A. A., Fairall, C. W., Hare, J. E., Edson, J. B., and Miller, S. D.	2003	Wind stress vector over ocean waves. *J. Phys. Oceanogr*., **33**, 2408-2429.
Gyakum, J. R, and Danielson, R. E.	2000	Analysis of meteorological precursors to ordinary and explosive cyclogenesis in the western North Pacific. *Mon. Weather Rev*., **128**, 851-863.
Haltiner, G. J.	1967	The effect of sensible heat exchange on the dynamics of baroclinic waves. *Tellus*, **19**, 183-198.
Hare, J. E., Persson, P. O. G., Fairall, C. W., and Edson, J. B.	1999	Behavior of Charnock's relationship for high wind conditions. *Preprints, 13th Symp. on Bound. Layers and Turbulence*, Jan. 10-15, 1999, Dallas, TX, 252-255.
Hare, J. E., Fairall, C. W., and Otten, J.	2000	Long term measurement of turbulent fluxes at sea. *Preprints, 14th Symp. on Boundary Layer and Turbulence*, 7-11 August 2000, Aspen, CO, 514-517.
Hauser, D., Branger, H., Bouffiès-Cloché, S., Despiau, S., Drennan, W., Dupuis, H., Durand, P., Durieu de Madron, X.,Estournel, C., Eymard, L., Flamant, C., Graber, H., Guérin, C., Kahma, K., Lachaud, G., Lefevre, J. M., Pelon, J., Pettersen, H., Piguet, B., Queffeulou, P., Taillez, D., Tournadre, J., and Weill, A.	2003	The FETCH experiment: an overview. *J. Geophys. Res*., **108 (C3)**, 8053, doi:10.1029/2001JC001202.
Hobbs, P. V., Matejka, T. J., Herzegh, P. H., Locatelli, J. D., R. A. Jr.	1980:	The mesoscale and microscale structure and organization of clouds and precipitation in Houze, midlatitude cyclones. Part I: A case study of a cold front. *J. Atmos. Sci*., **37**, 568-596.

Janssen, P. A. E. M.	1999	On the effect of ocean waves on kinetic energy balance and consequences for the inertial dissipation technique. *J. Phys. Oceanogr.*, **29**, 530-534.
Janssen, P. A. E. M.	2001	Reply. *J. Phys. Oceanogr.*, **31**, 2537-2544.
Joly, A., and Thorpe, A. J.	1990	Frontal instability generated by tropospheric potential vorticity anomalies. *Quart. J. Roy. Meteor. Soc.*, **116**, 525-560.
Joly, A., Browning, K. A., Bessemoulin, P., Cammas, J.-P., Caniaux, G., Chalon, J.-P., Clough, S. A., Dirks, R., Emanuel, K. A., Eymard, L., Gall, R., Hewson, T., Hildebrand, P. H., Jorgensen, D., Lalaurette, F., Langland, R. H., Lemaître, Y., Mascart, P., Moore, J. A., Persson, P. O. G., Roux, F., Shapiro, M. A., Snyder, C., Toth, Z., and Wakimoto, R.	1999:	Overview of the field phase of the Fronts and Atlantic Storm-Track Experiment (FASTEX) project. *Q. J. R. Meteorol. Soc.*, **125**, 3131-3163.
Joly, A., Jorgensen, D., Shapiro, M. A., Thorpe, A., Bessemoulin, P., Browning, K. A., Cammas, J.-P., Chalon, J.-P., Clough, S. A., Emanuel, K. A., Eymard, L., Gall, R., Hildebrand, P. H., Langland, R. H., Lemaître, Y., Lynch, P., Moore, J. A., Persson, P. O. G., Snyder, C., and Wakimoto, R.	1996:	The Fronts and Atlantic Storm-Track Experiment (FASTEX): Scientific objectives and experimental design. *Bull. Amer. Meteor. Soc.*, **78**, 1917-1940.
Kondo, J.	1975	Air-sea bulk transfer coefficients in diabatic conditions. *Bound.-Layer Meteor.*, **9**, 91-112.
Kristensen, L., Mann, J., Oncley, S. P., and Wyngaard, J. C.	1997	How close is close enough when measuring scalar fluxes with displaced sensors?, *J. Atmos. Ocean. Technol.*, **14**, 814-821, 1997.
Kuo, Y-W., Reed, R. J., and Low-Nam, S.	1991	Effects of surface energy fluxes during the early development and rapid intensification stages of seven explosive cyclones in the Western Atlantic. *Mon. Weather Rev.*, **119**, 457-476.
Langland, R. H., Elsberry, R. L. and Errico, R. M.	1995:	Evaluation of physical processes in an idealized and extratropical cyclone using adjoint techniques. *Q. J. R. Meteorol. Soc.*, **121**, 1349-1386.

Large, W.G., and Pond, S. 1981 Open ocean momentum flux measurements in moderate to strong winds. *J. Phys. Oceanogr.*, **11**, 324-336.

Large, W.G., and Pond, S. 1982 Sensible and latent heat flux measurements over the ocean. *J. Phys. Oceanogr.*, **12**, 464-482.

Moat, B. I., and Yelland, M. J. 1998 Airflow distortion at instrument sites on the R/V *Knorr*. SOC Internal report, Southampton Oceanography Centre, Southampton, UK.

Neumann, G., and Pierson, W. J., Jr. 1966 *Principles of Physical Oceanography*, Prentice-Hall, Inc., Englewood Cliffs, N.J., 545 pp.

Persson, P. Ola G. 1995 Simulations of the potential vorticity structure and budget of FRONTS '87 IOP8. *Q. J. R. Meteorol. Soc.*, **121**, 1041-1081.

Ralph, F. M., Neiman, P. J., and Wick, G. A. 2004 Satellite and CALJET aircraft observations of atmospheric rivers over the eastern North Pacific Ocean during the winter of 1997/98. *Mon. Weather Rev.*, **132**, 1721-1745.

Reed, R. J., and Albright, M. D. 1986 A case study of explosive cyclogenesis in the eastern Pacific. *Mon. Weather Rev.*, **114**, 2297-2319.

Reed, R. J., and Simmons, A. J. 1991 An explosively deepening cyclone over the North Atlantic that was unaffected by concurrent surface energy fluxes. *Weather and Forecasting*, **6**, 117-122.

Rieder, K. F, Smith, J. A., and Weller, R. A. 1994 Observed directional characteristics of the wind, wind stress, and surface waves on the open ocean. *J. Geophys. Res*., **99**, C11, 22,589-22,596.

Rieder, K. F, and Smith, J. A. 1998 Removing wave effects from the wind stress vector. *J. Geophys. Res*., **103**, C1, 1363-1374.

Smith, S. D. 1980 Wind stress and heat flux over the ocean in gale force winds. *J. Phys. Oceanogr.*, **10**, 709-726.

Stoelinga, M. T. 1996 A potential-vorticity-based study of the role of diabatic heating and friction in a numerically simulated baroclinic cyclone. *Mon. Weather Rev.*, **124**, 849-874.

Taylor, P. K., and Yelland, M. A. 2001a Comments on "On the effect of ocean waves on the kinetic energy balance and consequences for the inertial dissipation technique. *J. Phys. Oceanogr*., **31**, 2532-2536.

Taylor, P. K., and Yelland, M. A. 2001b The dependence of sea surface roughness on the height and steepness of the waves. *J. Phys. Oceanogr*., **31**, 572-590.

Webb, E. K., Pearman, G. I., and Leuning, R. 1980 Correction of flux measurements for density effects due to heat and water vapor transport, *Q. J. R. Meteorol. Soc*., **106**, 85-100.

Webster, P. J., Bradley, E. F., Fairall, C. W., Godfrey, J. S., Hacker, P., Houze, R.A. Jr., Lukas, R., Serra, Y., Hummon, J. M., Lawrence, T. D. M., Russell, C. A., Ryan, M. N., Sahami, K., and Zuidema, P. 2002 The JASMINE pilot study. *Bull. Amer. Meteor. Soc.*, **83**, 1603-1630.

Weill, A., Eymard, L., Caniaux, G., Hauser, D., Planton, S., Dupuis, H., Brut, A., Guérin, C., Nacass, P., Butet, A., Cloché, S., Pedreros, R., Durand, P., Bourras, D., Giordani, H., Lachaud, G., and Bouhours, G. 2003 Toward a better determination of turbulent air-sea fluxes from several experiments. *J. Clim.*, **16**, 600-618.

Wernli, H. 1997 A Lagrangian-based analysis of extratropical cyclones. II: A detailed case-study. *Q. J. R. Meteorol. Soc*., **123**, 1677-1706.

White, A. B., Jordan, J. R., Martner, B. E., Ralph, F. M, and Bartram, B. W. 2000 Extending the dynamic range of an S-band radar for cloud and precipitation studies. *J. Atmos. Ocean. Technol*., **17**, 1226-1234.

Wilczak, J. M., Oncley, S. P., and Stage, S. A. 2001 Sonic anemometer tilt correction algorithms. *Bound.-Layer Meteorol*., **99**, 127-150.

Yelland, M. J., and Taylor, P. K. 1996 Wind stress measurements from the open ocean. *J. Phys. Oceanogr.*, **26**, 541-558.

Yelland, M. J., Moat, B. I., Pascal, R. W., and Berry, D. I. 2002 CFD model estimates of the airflow distortion over research ships and the impact on momentum flux measurements. *J. Atmos. Ocean. Technol.*, **19**, 1477-1499.

Yelland, M. J., Moat, B. I., Taylor, P. K., Pascal, R. W., Hutchings, J., and Cornell, V. C. 1998 Wind stress measurements from the open ocean corrected for airflow distortion by the ship. *J. Phys. Oceanogr.*, **28**, 1511-1526.

Young, G. S., Levina, D. R., and Fairall, C. W. 1992 Influence of precipitating convection on the surface energy budget observed during a Tropical Ocean Global Atmosphere pilot cruise in the tropical western Pacific Ocean. *J. Geophys. Res*., **97**, 9595-9603.

Zeng, X., Zhao, M., and Dickinson, E. 1998 Intercomparison of bulk aerodynamic algorithms for the computation of sea surface fluxes using the TOGA COARE data. *J. Clim.*, **11**, 2628-2644.

Zhang, D.-L., Radeva, E., and Gyakum, J. 1999 A family of frontal cyclones over the Western Atlantic Ocean. Part II: Parameter studies. *Mon. Weather Rev.*, **127**, 1745-1760.

TABLE 1. LIST OF INSTRUMENTS ON THE R/V *KNORR* DURING FASTEX

The second column shows the directly measured and derived parameters from each instrument. Column three shows the instrument heights for the in-situ sensors and the sampling heights for the remote sensors. The sampling rate is given in the fourth column, with the minimum stored resolution of the averaged data given in parentheses if different than the sampling rate. Use the last column and Figure 1 to locate the instrument on the ship.

Instrument	**Parameters Measured**	**Height (m) MSL**	**Sampling Rate**	**Instrument Location**
Gill-Solent, R2, ultrasonic anemometer/thermometer	u, v, w, WS, WD, τ, H_s, H_l, turb. spectra	19.2	20.83 Hz	bow mast
Ophir IR-2000 fast hygrometer	q', H_l	17.5	20 Hz	bow mast
Systron-Donner, Motion-Pak	sonic platform motion	0.5	10 Hz	bow mast
Väisälä HMP35 T/RH probe,	T, RH	17.3	10 s (1 min)	bow mast
ETL floating thermistor	T_s	-0.05	10 s (1 min)	sea surface
Lowrance Global Positioning System	lat, lon, course, speed	N/A	2 Hz	internal laboratory
NCAR optical raingauge	precip rate	20	10 s (1 min)	port side railing on bridge roof
Kiel gimbaled ship raingauge	precip rate	20	10min	center railing on bridge roof
TSK microwave wave-height altimeter	h_w, t_w	7	2 Hz	bow
Eppley PSP and PIR	Q_{si}, Q_{li}	12	10 s (1 min)	stern
IMET basic met (RM Young)	WS, WD, P, T, RH	20	15 s	forward mast
IMET ship intake T_s	T_s	-4	15 s	bow
OMEGA Rawinsondes	ws, wd, P, T, RH	2-12,000	1-6 hr	fan tail
ETL S-band radar	reflectivity, fall speeds	105-5000	30 s	stern
non-scanning lidar	aerosol scatt., cloud base height	30-8000	1 min	stern
gyro-stabilized 915 MHz wind profiler	u, v, w, C_n^2	500- 4000	6 min (30 min)	stern
FSSP, Optical array probes	particle size distribution	N/A	30 min	starboard railing on bridge roof
Video cameras - forward and downward looking	sea state, visibility			port side of bridge window and bow mast
Gyrocompass	heading			internal laboratory
cont. underway pCO_2 system (NOAA/AOML)	surface water and air pCO_2	-4 and 13.5	4.5 min	bow waterline
K Gill-system with "spray flinger", dry/wet bulb psychrometers, Lyman-alpha hygrometer	u, v, w, WS, WD, τ, H_s, H_l, turb. spectra	K-Gill: 19 spray flinger:18.4	20 Hz	bow mast
NOAA/ATDD fast hygrometer and CO_2 sensor	q', H_l, CO_2	18.4	10 Hz	bow mast
Range-gated X-band radar	directional wave height spectra	0	5 s	main mast

TABLE 2. CHARACTERISTICS OF THE FASTEX CASES USED FOR COMPOSITING THE R/V *KNORR* DATA

Case	Warm sector duration (hr)	Cold-frontal passage (decimal Julian Day)	Post-frontal baroclinic regime duration (hr)	System phase velocity (m s^{-1}/ deg)	15-min, 19-m LLJ wind speed max (m s^{-1})	Avg. SST (deg C)
1	16.44	4.885	3.48	18.4/210	21.5	15.0
2	3.12	5.190	15.84	11.6/225	19.1	15.4
3	18.62	7.776	6.58	18.7/254	19.6	17.4
4	14.28	8.995	3.48	33.4/240	19.0	17.4
5	3.50	9.425	2.76	26.4/233	21.3	17.3
6	7.92	12.99	4.80	25.0/258	18.6	15.4
7	43.44	20.21	16.08	23.2/229	20.0	14.5
8	15.36	22.05	13.20	27.4/234	18.3	3.4
9	28.32	24.08	12.48	25.7/266	18.0	4.0
10	25.68	26.37	5.52	27.3/234	22.0	3.2
Average	17.7	N/A	8.4	23.7/238	19.7	16.1/3.5*

*The two averages in the last column are the average SSTs for the first seven and last three cases, respectively.

FIGURE CAPTIONS

Figure 1. Placement of instrumentation onboard the R/V *Knorr* as viewed from (a) in front of the ship, (b) the bridge toward the bow, and (c) the bridge toward the stern.

Figure 2. Methodology for calculating wave height and wave period. The solid curve shows the output from the TSK wave-height recorder from 1115 – 1118 UTC Jan. 2. See text for discussion.

Figure 3. Track of R/V *Knorr* (dark line) during the FASTEX experiment from Dec 23, 1996, to Jan 26, 1997. The tracks are marked with an "x" every 12 hours, and are labeled with the day of the month at 00 UTC. Also shown is the sea-surface temperature analysis (grey lines, K) from ECMWF on January 7, 1997. The observed strong SST gradient of the Gulf Stream "wall" is bracketed by the two vertical lines along the ship track at times JD20.75 and JD21.67. The open circles show the location of the *Knorr* at the time of the cold-frontal passages discussed in sections 4-6 and listed in Table 2.

Figure 4. Surface pressure and 19-m wind speeds from the R/V *Knorr* during its FASTEX cruise. The wind speeds from both the Athena system (solid) and the NOAA/ETL sonic anemometer (dots) are shown. The double-headed arrows show the times of each storm or frontal wave.

Figure 5. Characterization of the data sampled from the R/V *Knorr* showing (a) the number of occurrences of each hourly 1-m/s wind speed bin, and (b) the air-sea temperature difference associated with each hourly wind speed measurement. 344 hours were collected to the east of the Gulf Stream wall [dots in (b)] and 59 hours to the west of it [x in (b)]. Only points for which the ship was stationary and facing into the wind with the sonic anemometer operational are shown.

Figure 6. Scatter plot of stability parameter z/L versus wind speed for the hourly samples from the R/V *Knorr* for which the stress, sensible heat, and latent heat fluxes were all available. There are 289 points.

Figure 7. Scatter plot of hourly averaged (a) streamwise covariance stress (τ_{sc}), and (b) cross-stream covariance stress (τ_{cc}) as a function of the 10-m neutral wind speed. Also shown are bin-averaged values for 1 m s^{-1} wind speed bins (squares).

Figure 8. The bin-median values of the 10-m neutral transfer coefficients for (a) momentum, (b) sensible heat, and (c) latent heat as a function of the 10-m neutral wind speed from the covariance (square) and ID (triangle) techniques. The linear fits to the average of the two methods is shown as a heavy dashed line. Only bins with at least 18 10-minute data points are shown, and the error bars show one standard deviation about the ID values. Additional curves are from Fairall *et al.* (2003; FR03, gray solid), Eymard *et al.* [1999; EY99, dotted in (a) and (c)], Dupuis *et al.* [1997; DU97, dotted in (b)], Janssen [1999; J99, dash - double dot in (a)], Dupuis *et al.* [2003; DU03, thin solid in (c)], and Dobson *et al.* [1994; DP94, dash-dot in (a)]. The

shaded area in (a) represents the region of numerous other curves, primarily from ID measurements as described in the text.

Figure 9. Scatter plots of (a) significant (x) and maximum (dots) wave heights, and (b) significant (x) and maximum (dots) wave period as a function of wind speed. Bin averaged values for 1 m s^{-1} wind speed bins are blue squares and diamonds, respectively. The wave heights and wave periods in equilibrium with the given wind speed are shown as bold dashed curves (from Taylor and Yelland 2001b). Only hours for which covariance stresses were obtained are shown.

Figure 10. Scatter plots of hourly values of streamwise stress as a function of (a) significant wave height, and (b) significant wave period. Bin-averaged values are shown as squares.

Figure 11. Time series of (a) specific humidity (x) and wind direction (dot), (b) 19-m wind speed, (c) the air temperature (x) and the SSTs from the thermosalinograph (dots) and the seasnake (diamonds), and (d) surface pressure (solid) and rain rate (dashed) from the R/V *Knorr* for case 4 (JD8.25-9.25). The onset of the warm sector (WSB), the cold-frontal passage (CFP), and the end of the post-frontal regime (PFE) are marked by dashed and solid vertical lines. Note that time runs from right to left in order to place the warm sector to the right of the cold front.

Figure 12. Time-to-space converted tracks of the research vessels *Knorr* (x), *Aegir* (A), *Victor Bugaev* (B), and *Suroit* (S) for cases 3, 4, 6 and 8. The overlaid infrared satellite image corresponds to a time shortly prior to when the R/V *Knorr* passed through the surface cold front. The time next to each symbol marks the hour (UTC) at that location.

Figure 13. Composite relative values of (a) temperature, (b) specific humidity, (c) wind speed, and (d) wind direction with respect to the cold frontal passage from the R/V *Knorr*. Values are relative to their values at the onset of the warm sector, except for wind direction, which is relative to the value 1 hour before frontal passage. The stars show the data from the ETL sensors and the squares those from the ship's Athena data system. The 'x's show ±1 standard deviation of the Athena data. The numbers along the top and bottom of each frame show the number of cases that contributed to each composite bin for the ETL and Athena sensors, respectively.

Figure 14. Composite values of (a) significant (stars) and maximum (squares) wave heights and their ratio (diamonds), (b) significant wave period , (c) wave frequency for different wave period bins, and (d) wave height for different wave period bins with respect to the cold frontal passage from the R/V *Knorr*. The wave period bins in (c) and (d) are 0-3.4 s (stars), 3.4-6.4 s, (squares), 6.4-9.5 s (diamonds), and 9.5-12.6 s (circles).

Figure 15. Composite values of (a) stress, (b) sensible heat flux, and (c) latent heat flux determined from the covariance method with respect to the cold frontal passage from the R/V *Knorr*. Panel (d) shows the composite of the difference between the stress direction and wind direction. A 3-point running mean was applied to the stress components before the stress direction was calculated. The vertical errors bars show ± one standard deviation.

Figure 16. Time series from the R/V *Knorr* of wind direction (line), stress direction (*), and manual observations of the swell direction from two different ship logs (diamond, x) for the period Julian Day 7.3 – 9.25. The two vertical dashed lines show the cold-frontal passages for

cases 3 and 4 (CFP3, CFP4), the long and double-short dash line the WSB for case 4, and the dash-dot lines the two PFE.

Figure 17. (a)-(c) Same as Fig. 15, but for fluxes calculated from the inertial dissipation technique. In (d), the differences between the covariance and ID values of stress (solid), H_s (dashed) and H_l (dot-dash) are shown. Note that the stress differences have been multiplied by 500 to scale properly on the plot.

Figure 18. Composites of (a) stress, (b) sensible heat flux, and (c) latent heat flux calculated from the bulk formulas of Fairall *et al.* (2003). In (d), the differences between the covariance and bulk values of stress (heavy solid), H_s (dash) and H_l (thin solid) are shown. Note that the stress differences have been multiplied by 500 to scale properly on the plot.

Figure 19. Schematic diagram summarizing the composite variations of (a) the atmospheric constituents, and (b) the surface fluxes and ocean waves relative to the warm sector, cold front, and post-frontal regions. T_a, q_a, WS, H_s, H_l, τ, and h_s represent atmospheric temperature, atmospheric water vapor, wind speed, sensible heat flux, latent heat flux, stress, and significant wave height, respectively. The solid arrows show wind direction and the dashed arrows in (b) show stress direction. The region representing the atmospheric water vapor plume is shaded.

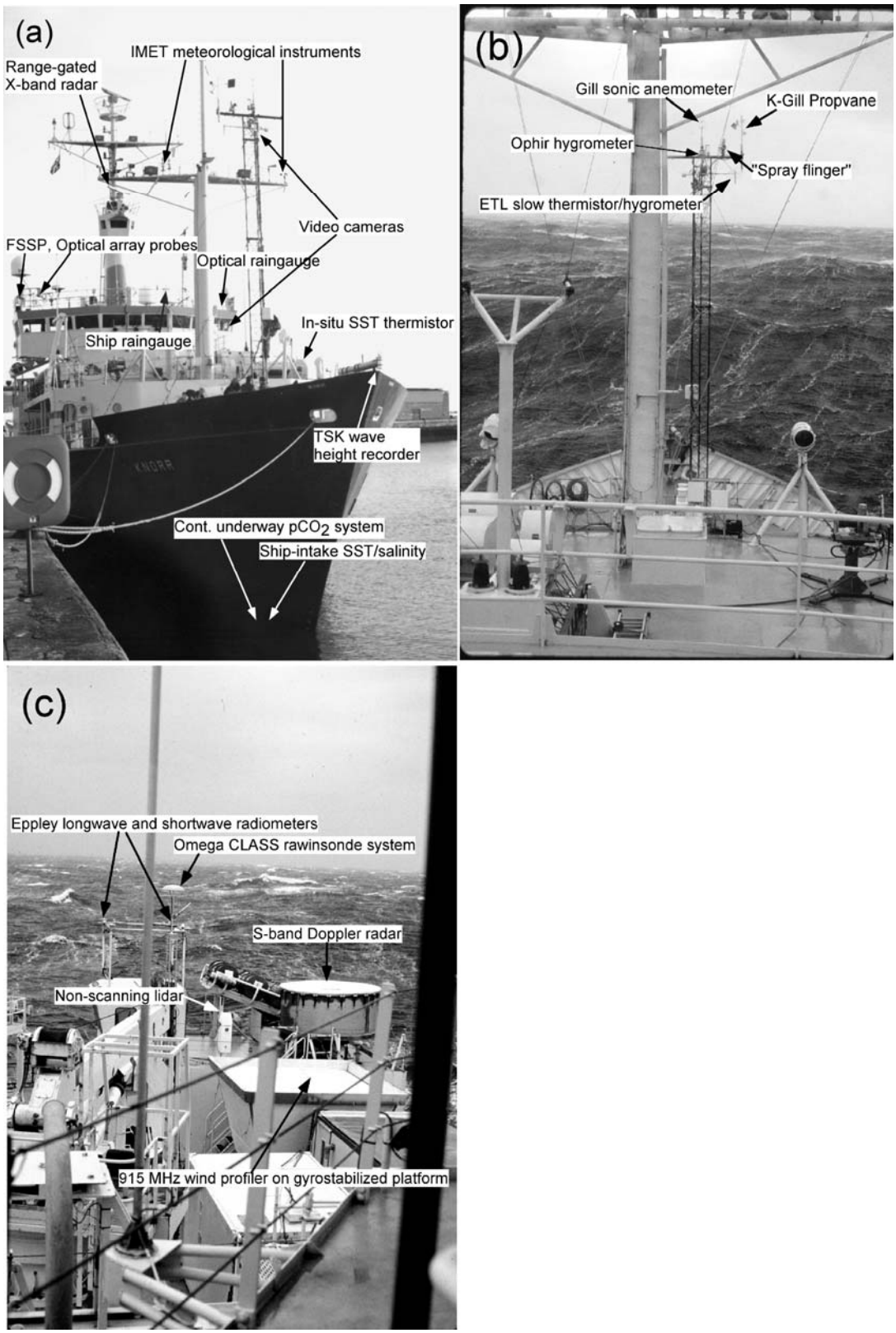

Figure 1. Placement of instrumentation onboard the R/V *Knorr* as viewed from (a) in front of the ship, (b) the bridge toward the bow, and (c) the bridge toward the stern.

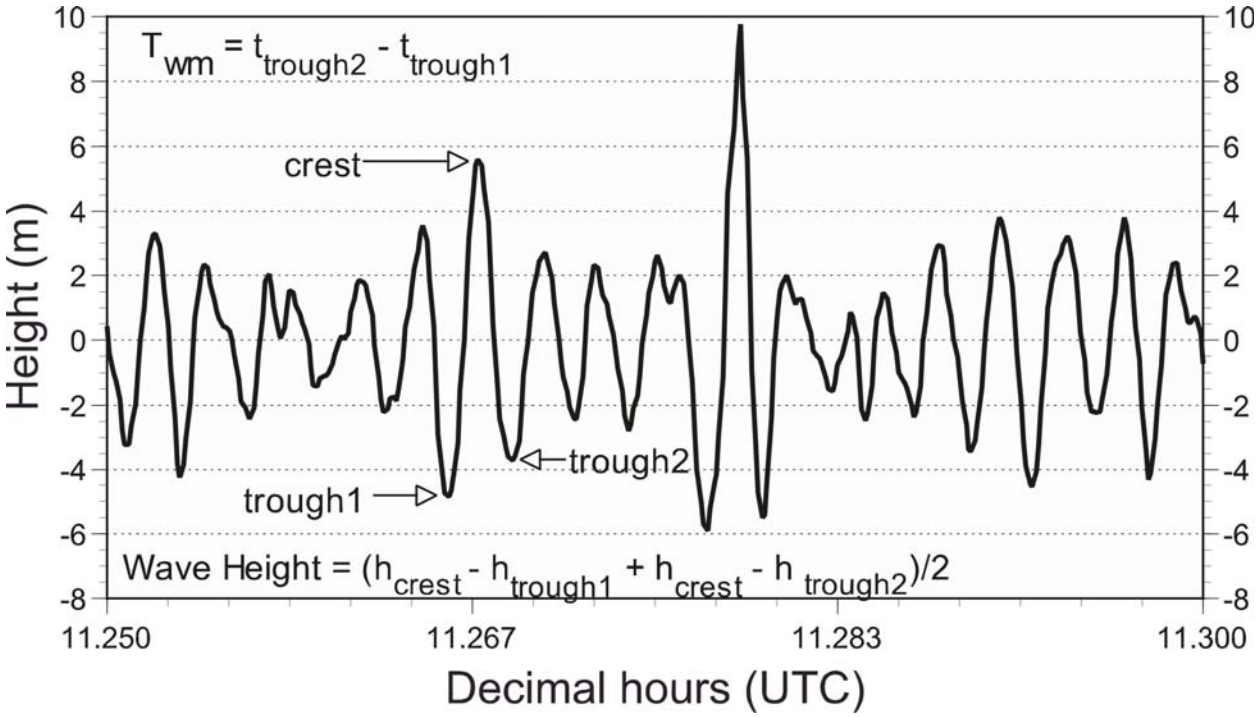

Figure 2. Methodology for calculating wave height and wave period. The solid curve shows the output from the TSK wave-height recorder from 1115 – 1118 UTC Jan. 2. See text for discussion.

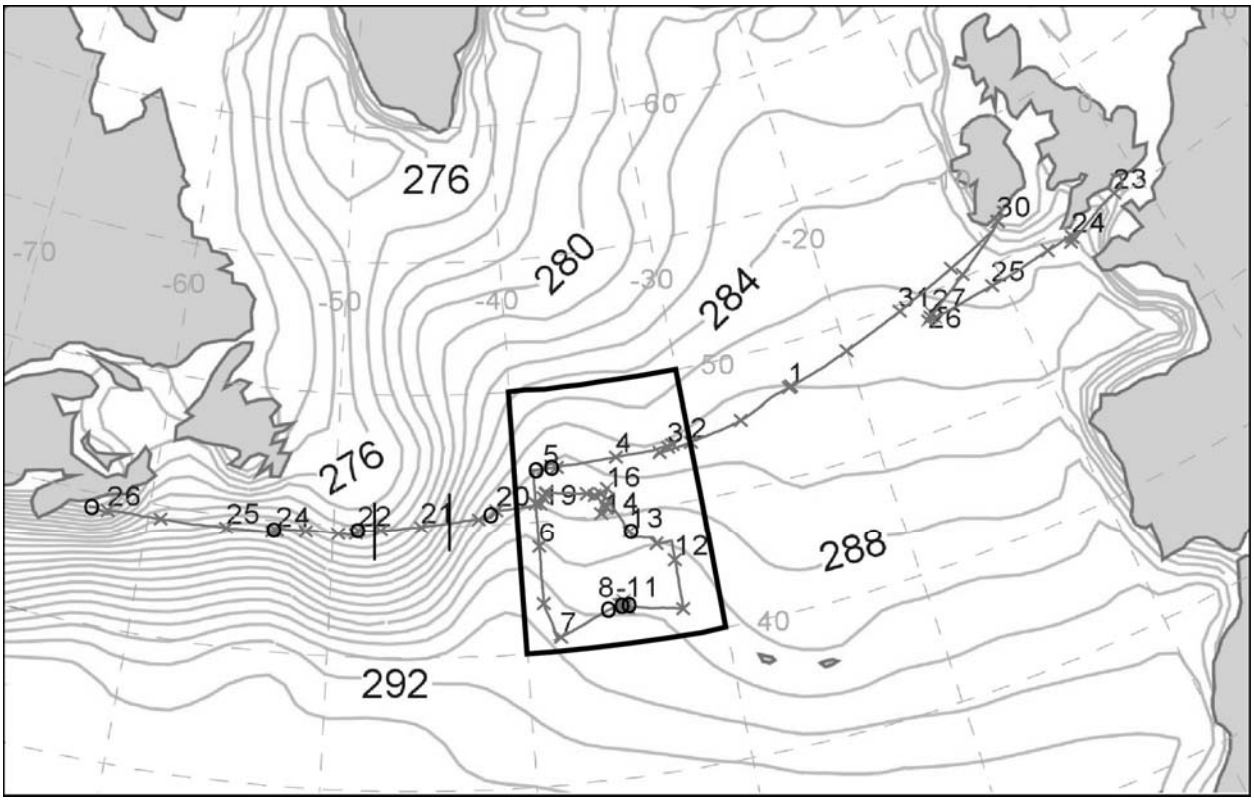

Figure 3. Track of R/V *Knorr* (dark line) during the FASTEX experiment from Dec 23, 1996, to Jan 26, 1997. The tracks are marked with an "x" every 12 hours, and are labeled with the day of the month at 00 UTC. Also shown is the sea-surface temperature analysis (grey lines, K) from ECMWF on January 7, 1997. The observed strong SST gradient of the Gulf Stream "wall" is bracketed by the two vertical lines along the ship track at times JD20.75 and JD21.67. The open circles show the location of the *Knorr* at the time of the cold-frontal passages discussed in sections 4-6 and listed in Table 2.

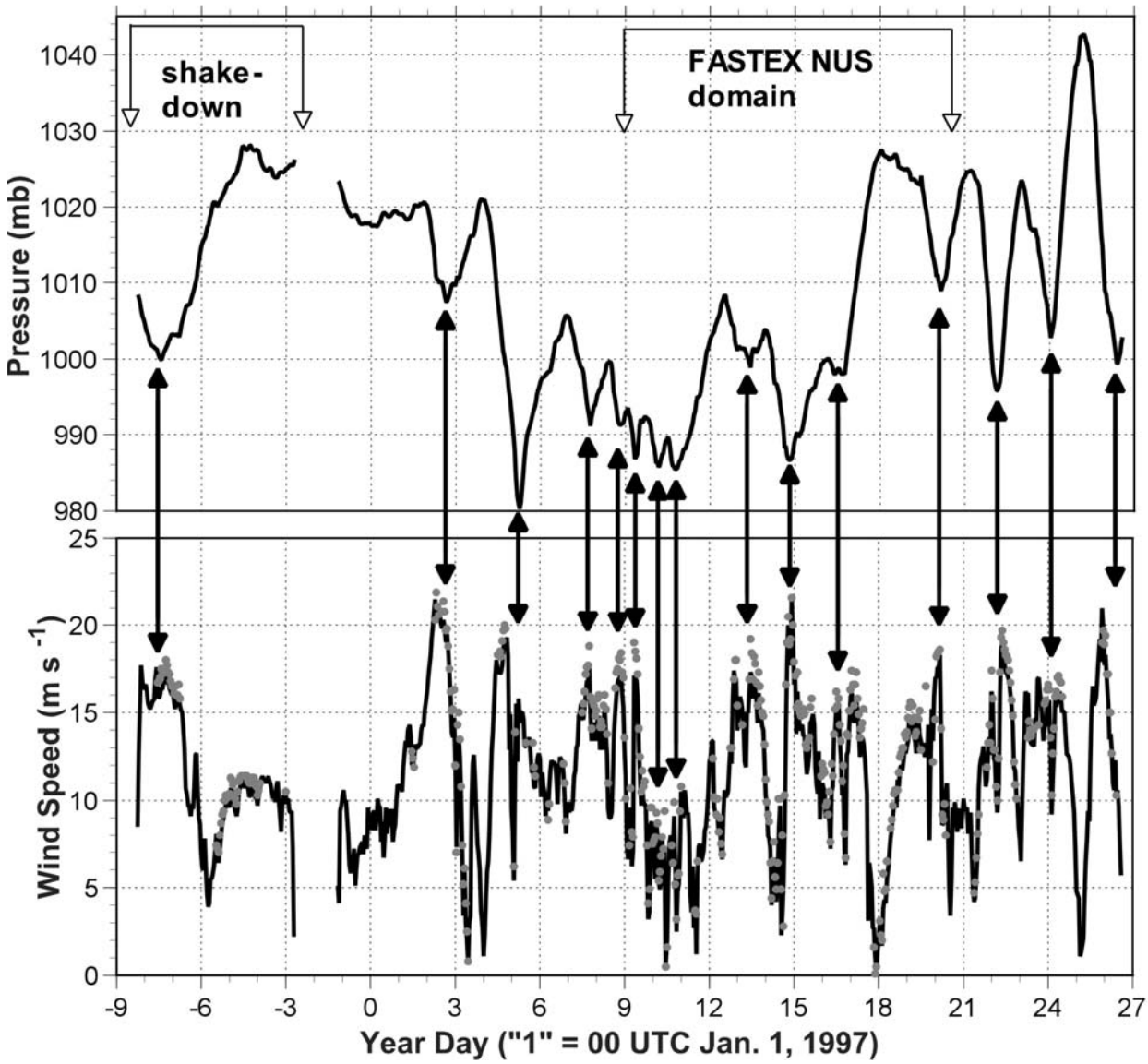

Figure 4. Surface pressure and 19-m wind speeds from the R/V *Knorr* during its FASTEX cruise. The wind speeds from both the Athena system (solid) and the NOAA/ETL sonic anemometer (dots) are shown. The double-headed arrows show the times of each storm or frontal wave.

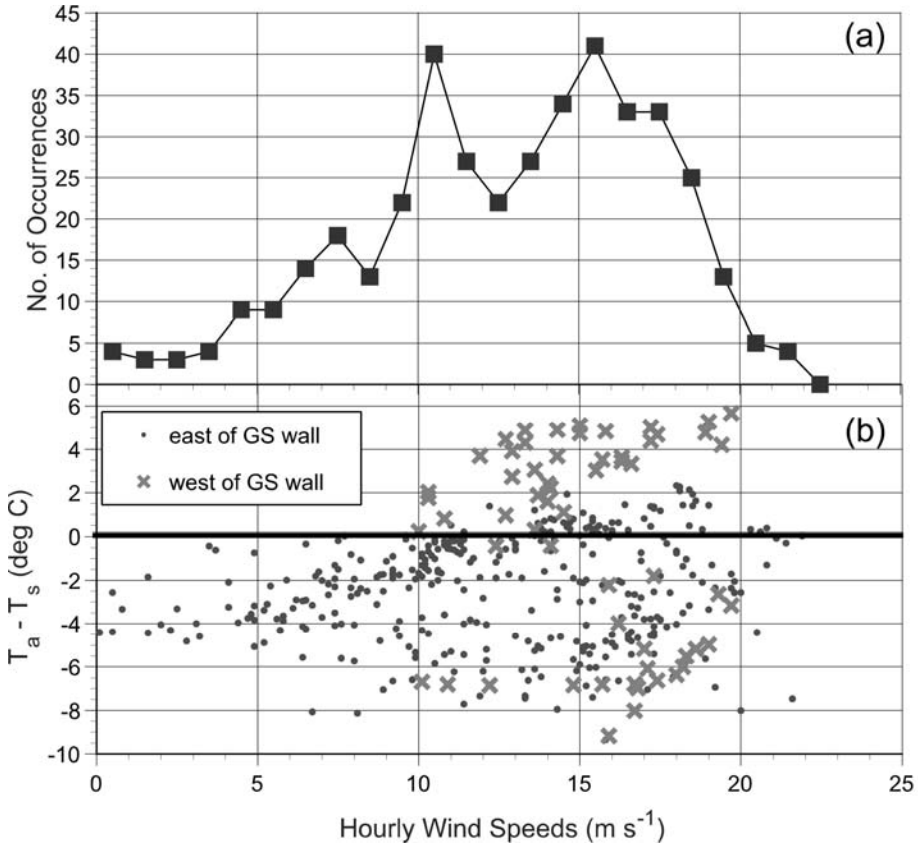

Figure 5. Characterization of the data sampled from the R/V *Knorr* showing (a) the number of occurrences of each hourly 1-m/s wind speed bin, and (b) the air-sea temperature difference associated with each hourly wind speed measurement. 344 hours were collected to the east of the Gulf Stream wall [dots in (b)] and 59 hours to the west of it [x in (b)]. Only points for which the ship was stationary and facing into the wind with the sonic anemometer operational are shown.

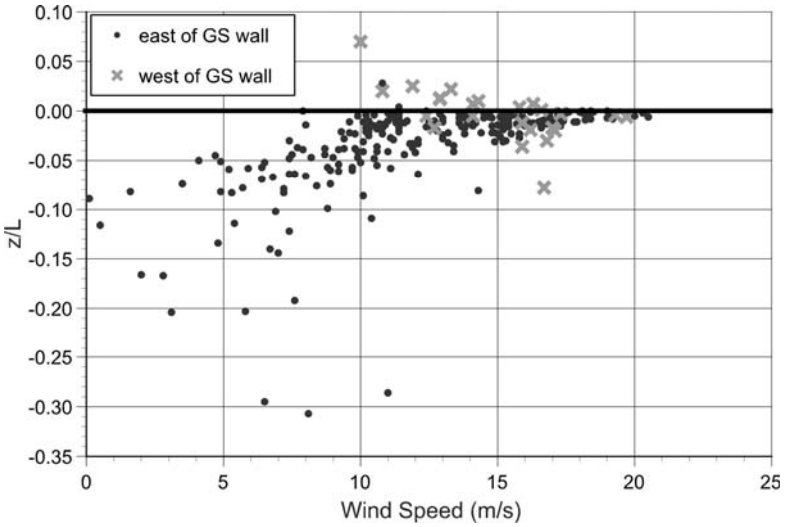

Figure 6. Scatter plot of stability parameter z/L versus wind speed for the hourly samples from the R/V *Knorr* for which the stress, sensible heat, and latent heat fluxes were all available. There are 289 points.

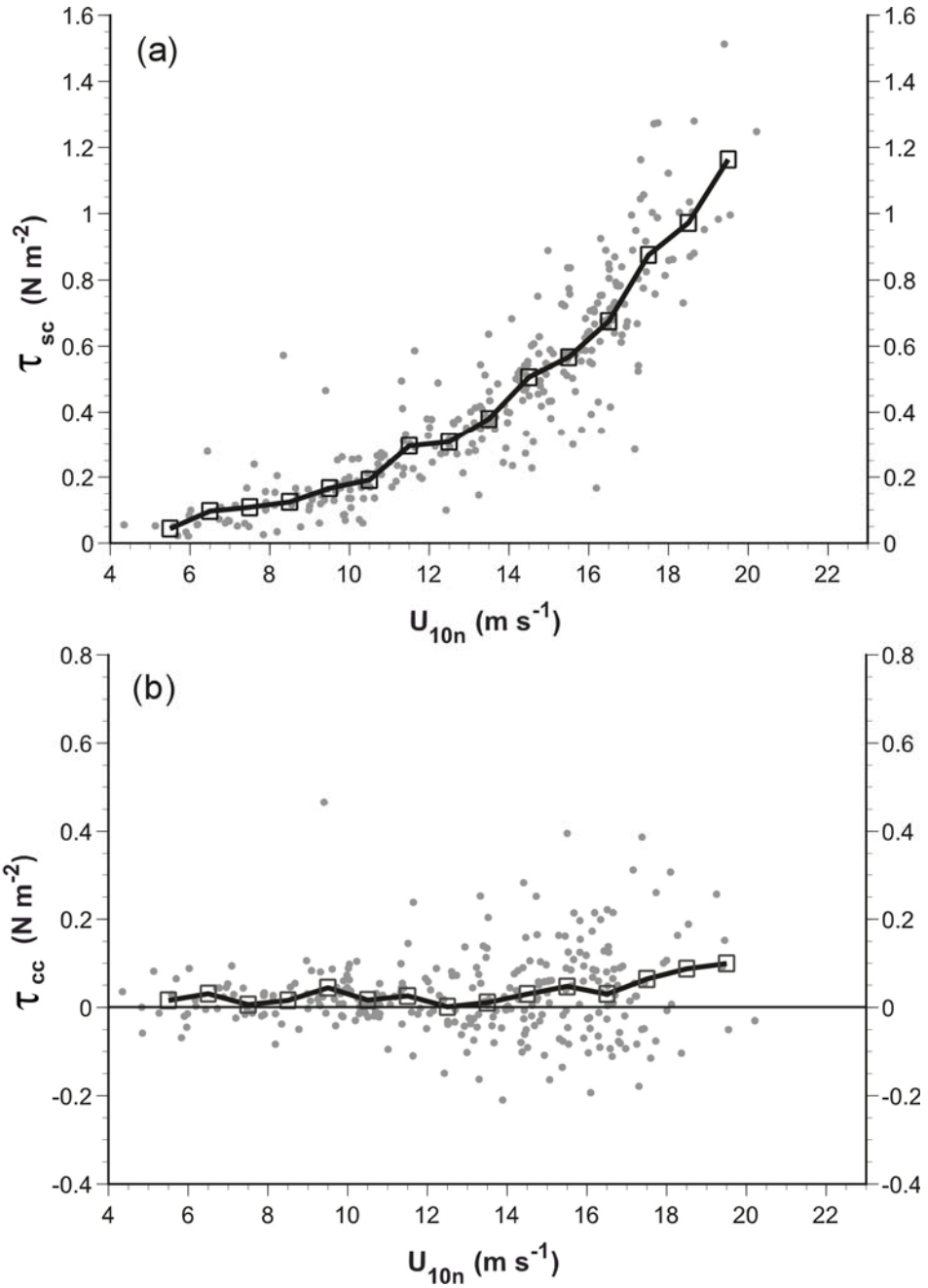

Figure 7. Scatter plot of hourly averaged (a) streamwise covariance stress (τ_{sc}), and (b) cross-stream covariance stress (τ_{cc}) as a function of the 10-m neutral wind speed. Also shown are bin-averaged values for 1 m s^{-1} wind speed bins (squares).

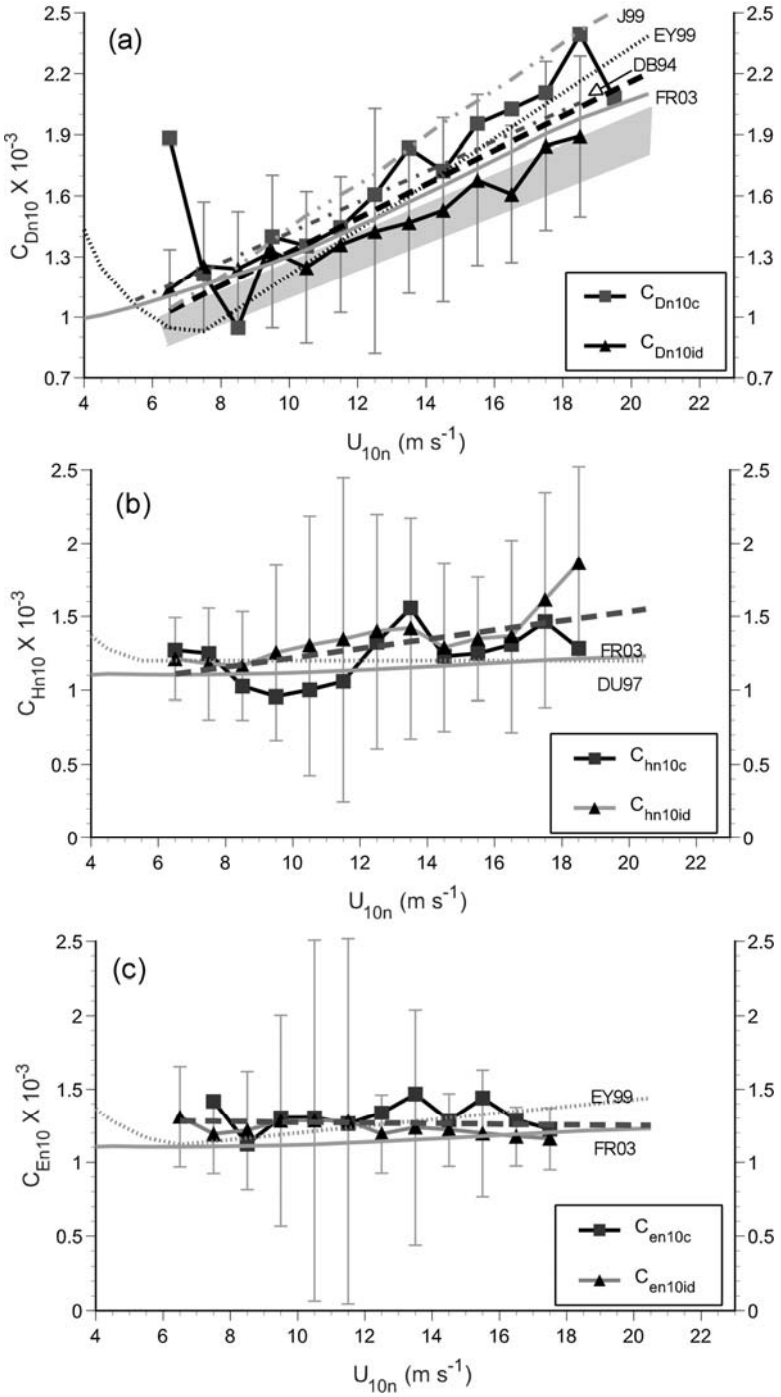

Figure 8. The bin-median values of the 10-m neutral transfer coefficients for (a) momentum, (b) sensible heat, and (c) latent heat as a function of the 10-m neutral wind speed from the covariance (square) and ID (triangle) techniques. The linear fits to the average of the two methods is shown as a heavy dashed line. Only bins with at least 18 10-minute data points are shown, and the error bars show one standard deviation about the ID values. Additional curves are from Fairall *et al.* (2003; FR03, gray solid), Eymard *et al.* [1999; EY99, dotted in (a) and (c)], Dupuis *et al.* [1997; DU97, dotted in (b)], Janssen [1999; J99, dash - double dot in (a)], Dupuis *et al.* [2003; DU03, thin solid in (c)], and Dobson *et al.* [1994; DP94, dash-dot in (a)]. The shaded area in (a) represents the region of numerous other curves, primarily from ID measurements as described in the text.

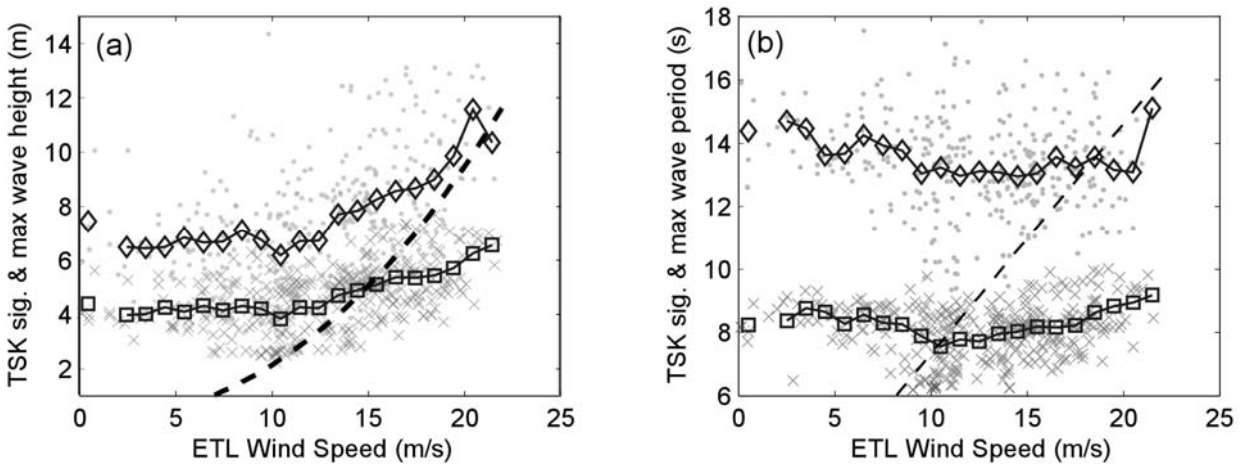

Figure 9. Scatter plots of (a) significant (x) and maximum (dots) wave heights, and (b) significant (x) and maximum (dots) wave period as a function of wind speed. Bin averaged values for 1 m s^{-1} wind speed bins are blue squares and diamonds, respectively. The wave heights and wave periods in equilibrium with the given wind speed are shown as bold dashed curves (from Taylor and Yelland 2001b). Only hours for which covariance stresses were obtained are shown.

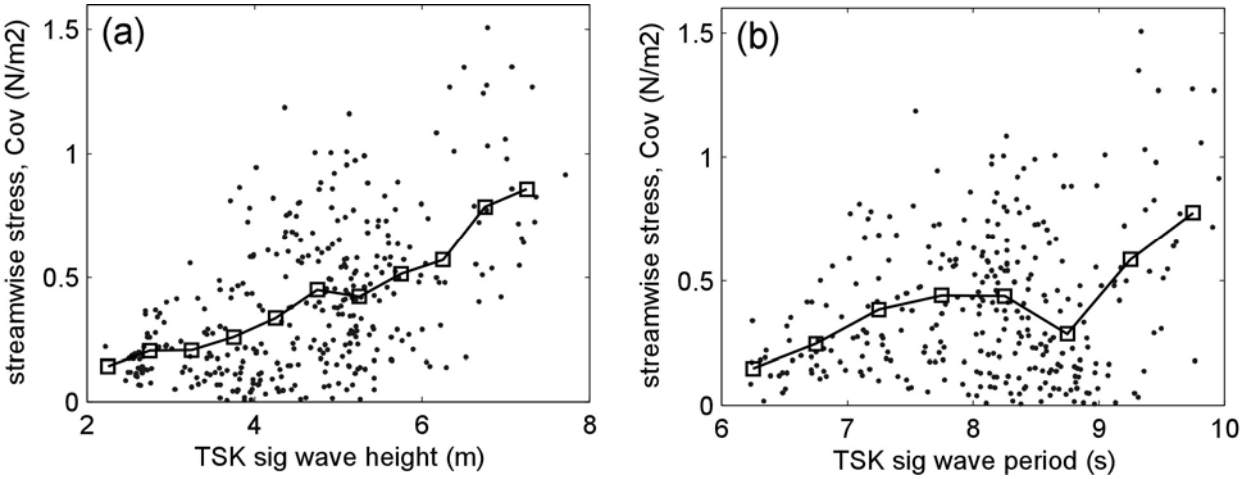

Figure 10. Scatter plots of hourly values of streamwise stress as a function of (a) significant wave height, and (b) significant wave period. Bin-averaged values are shown as squares.

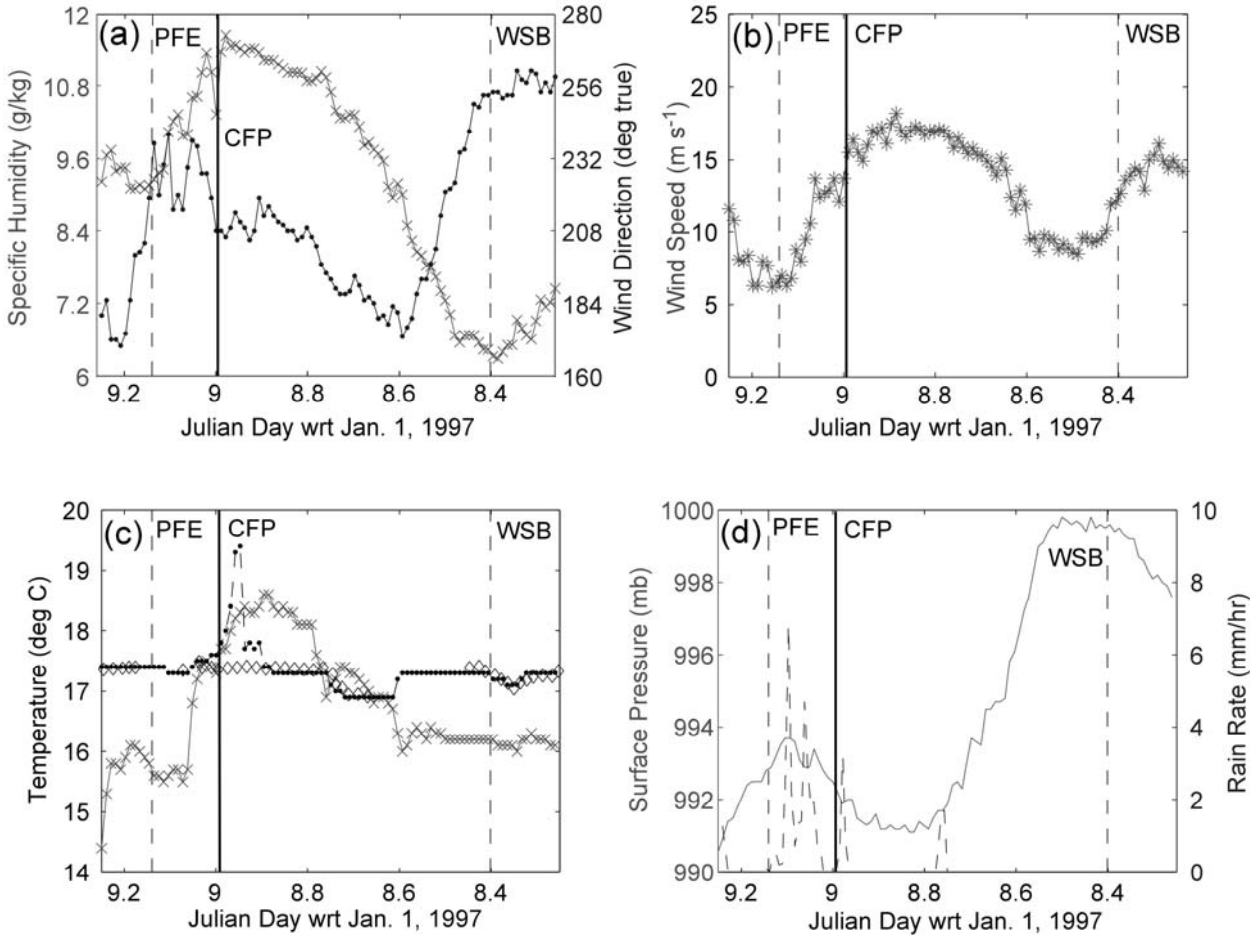

Figure 11. Time series of (a) specific humidity (x) and wind direction (dot), (b) 19-m wind speed, (c) the air temperature (x) and the SSTs from the thermosalinograph (dots) and the seasnake (diamonds), and (d) surface pressure (solid) and rain rate (dashed) from the R/V *Knorr* for case 4 (JD8.25-9.25). The onset of the warm sector (WSB), the cold-frontal passage (CFP), and the end of the post-frontal regime (PFE) are marked by dashed and solid vertical lines. Note that time runs from right to left in order to place the warm sector to the right of the cold front.

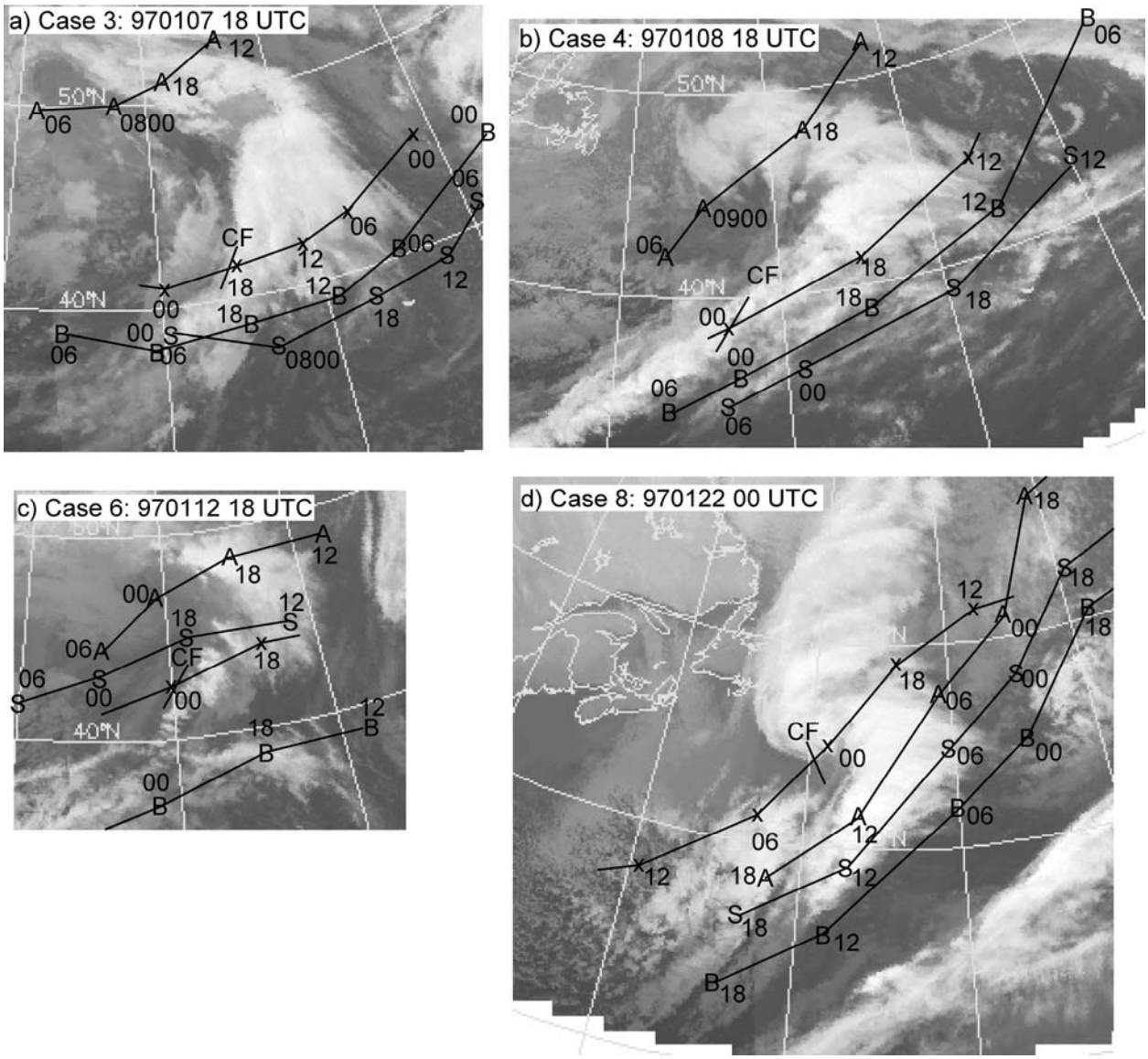

Figure 12. Time-to-space converted tracks of the research vessels *Knorr* (x), *Aegir* (A), *Victor Bugaev* (B), and *Suroit* (S) for cases 3, 4, 6 and 8. The overlaid infrared satellite image corresponds to a time shortly prior to when the R/V Knorr passed through the surface cold front. The time next to each symbol marks the hour (UTC) at that location.

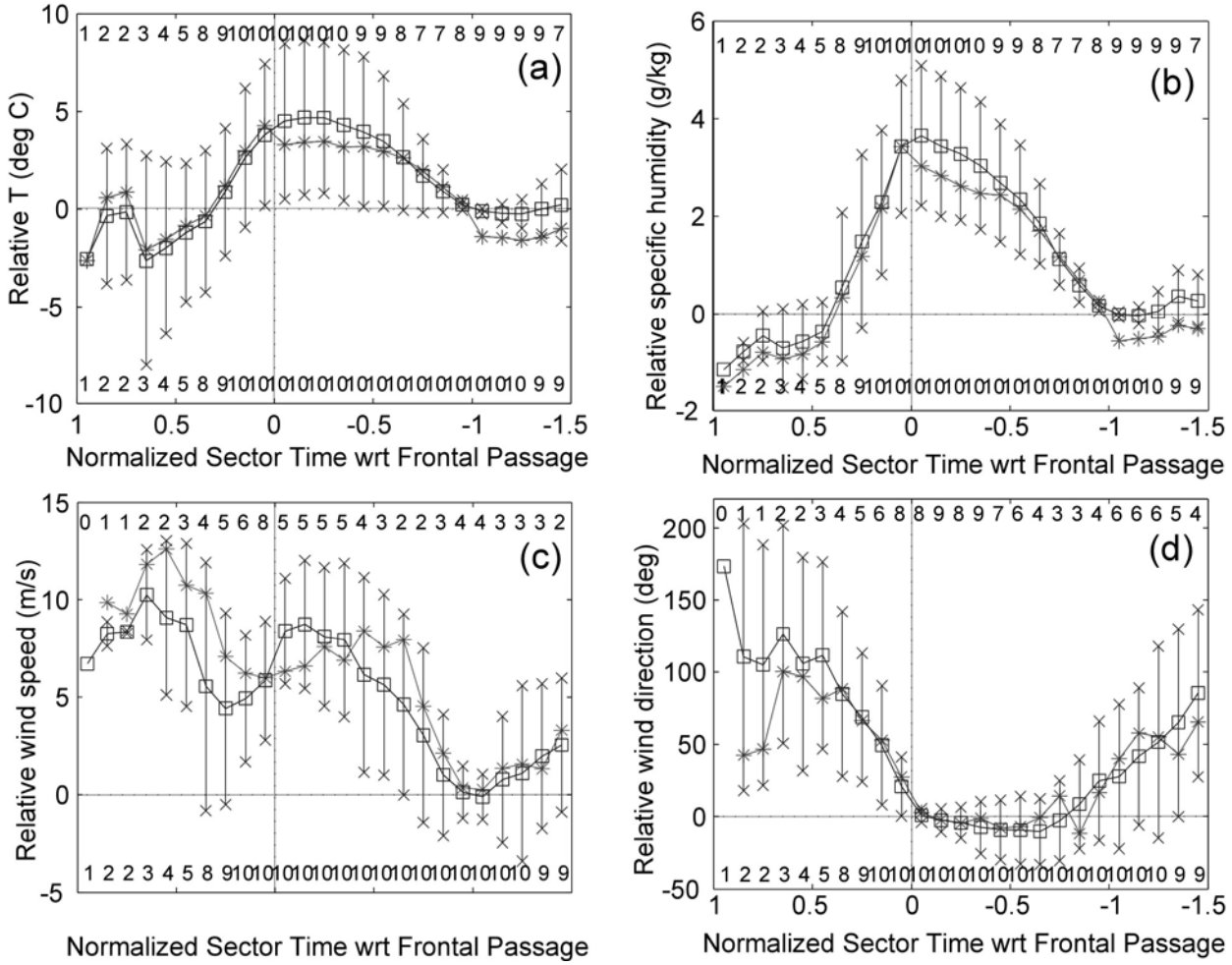

Figure 13. Composite relative values of (a) temperature, (b) specific humidity, (c) wind speed, and (d) wind direction with respect to the cold frontal passage from the R/V *Knorr*. Values are relative to their values at the onset of the warm sector, except for wind direction, which is relative to the value 1 hour before frontal passage. The stars show the data from the ETL sensors and the squares those from the ship's Athena data system. The 'x's show ±1 standard deviation of the Athena data. The numbers along the top and bottom of each frame show the number of cases that contributed to each composite bin for the ETL and Athena sensors, respectively.

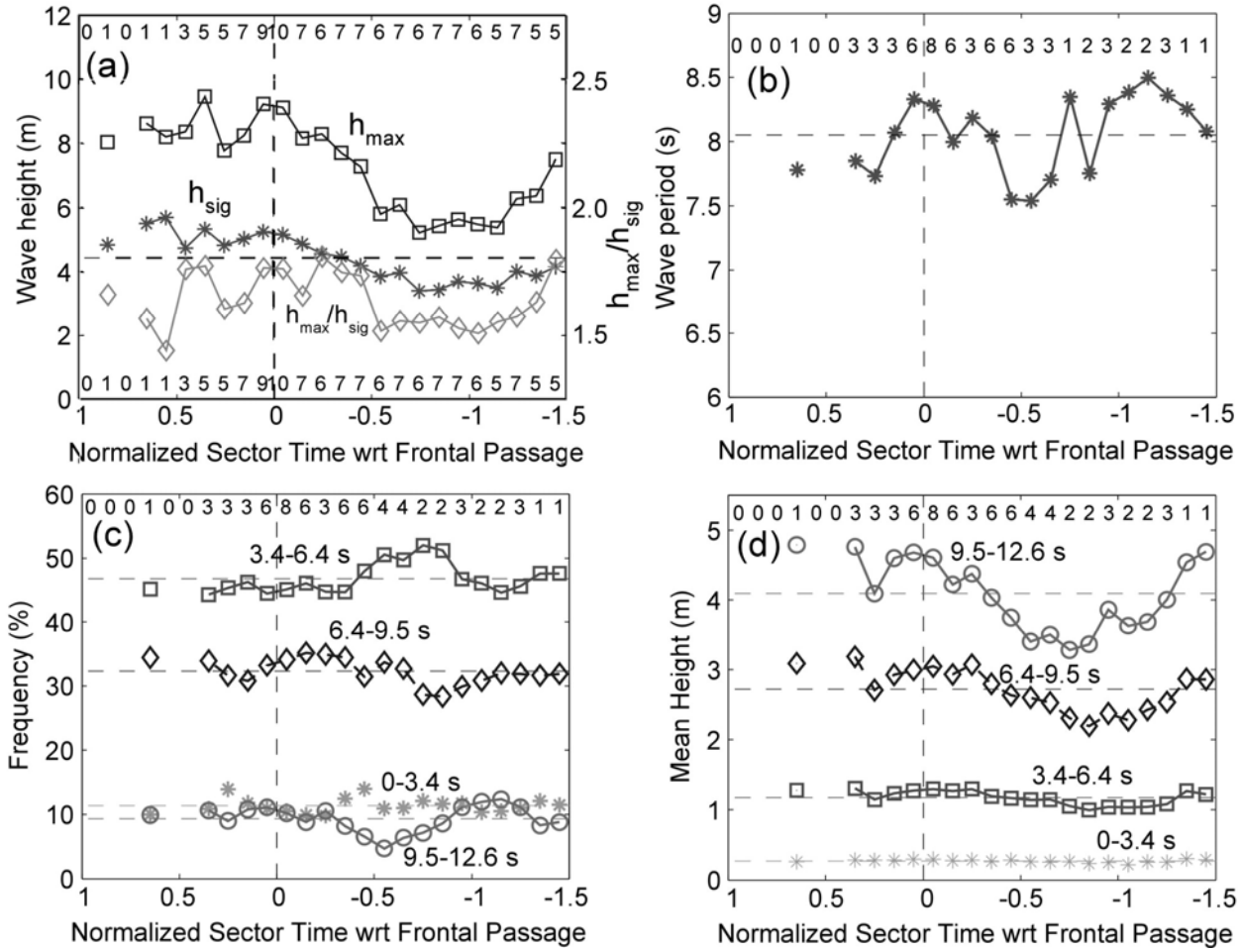

Figure 14. Composite values of (a) significant (stars) and maximum (squares) wave heights and their ratio (diamonds), (b) significant wave period , (c) wave frequency for different wave period bins , and (d) wave height for different wave period bins with respect to the cold frontal passage from the R/V *Knorr*. The wave period bins in (c) and (d) are 0-3.4 s (stars), 3.4-6.4 s, (squares), 6.4-9.5 s (diamonds), and 9.5-12.6 s (circles).

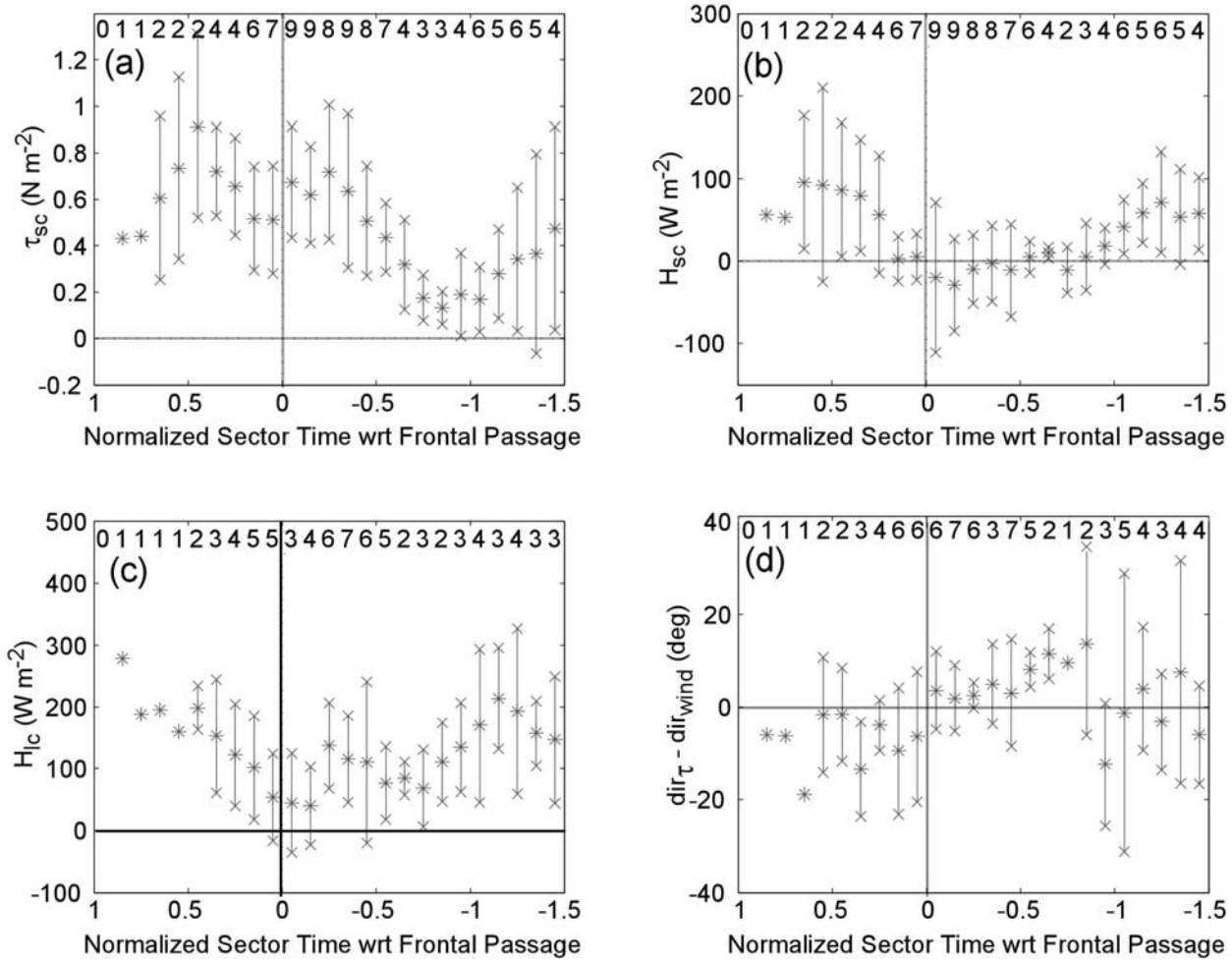

Figure 15. Composite values of (a) stress, (b) sensible heat flux, and (c) latent heat flux determined from the covariance method with respect to the cold frontal passage from the R/V *Knorr*. Panel (d) shows the composite of the difference between the stress direction and wind direction. A 3-point running mean was applied to the stress components before the stress direction was calculated. The vertical errors bars show ± one standard deviation.

.

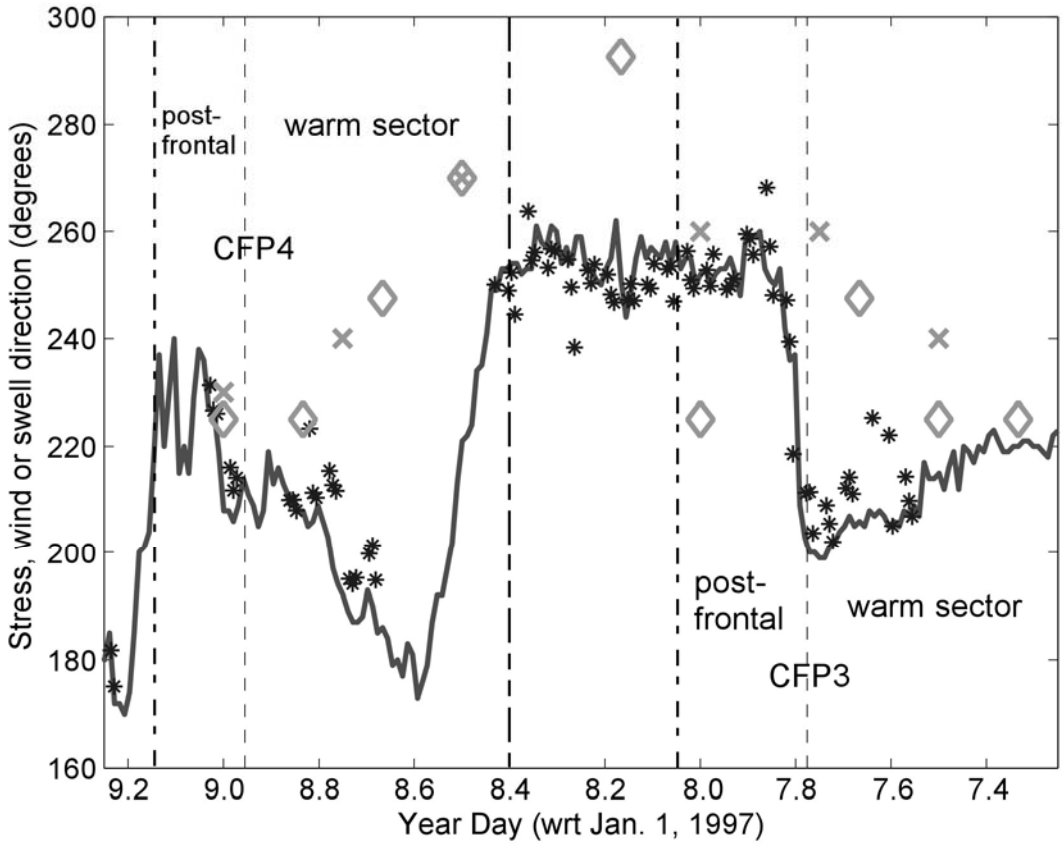

Figure 16. Time series from the R/V *Knorr* of wind direction (line), stress direction (*), and manual observations of the swell direction from two different ship logs (diamond, x) for the period Julian Day 7.3 – 9.25. The two vertical dashed lines show the cold-frontal passages for cases 3 and 4 (CFP3, CFP4), the long and double-short dash line the WSB for case 4, and the dash-dot lines the two PFE.

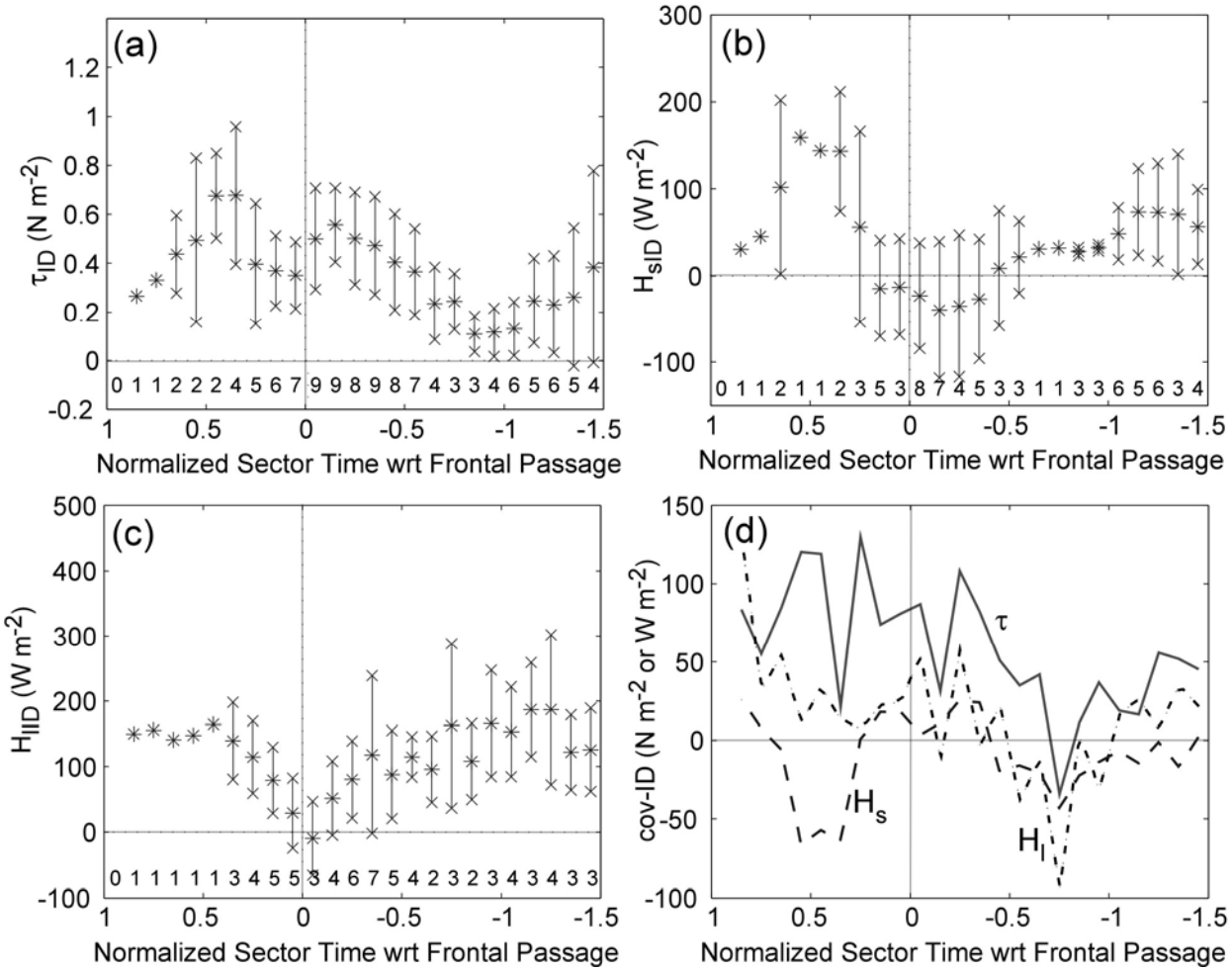

Figure 17. (a)-(c) Same as Fig. 15, but for fluxes calculated from the inertial dissipation technique. In (d), the differences between the covariance and ID values of stress (solid), H_s (dashed) and H_l (dot-dash) are shown. Note that the stress differences have been multiplied by 500 to scale properly on the plot.

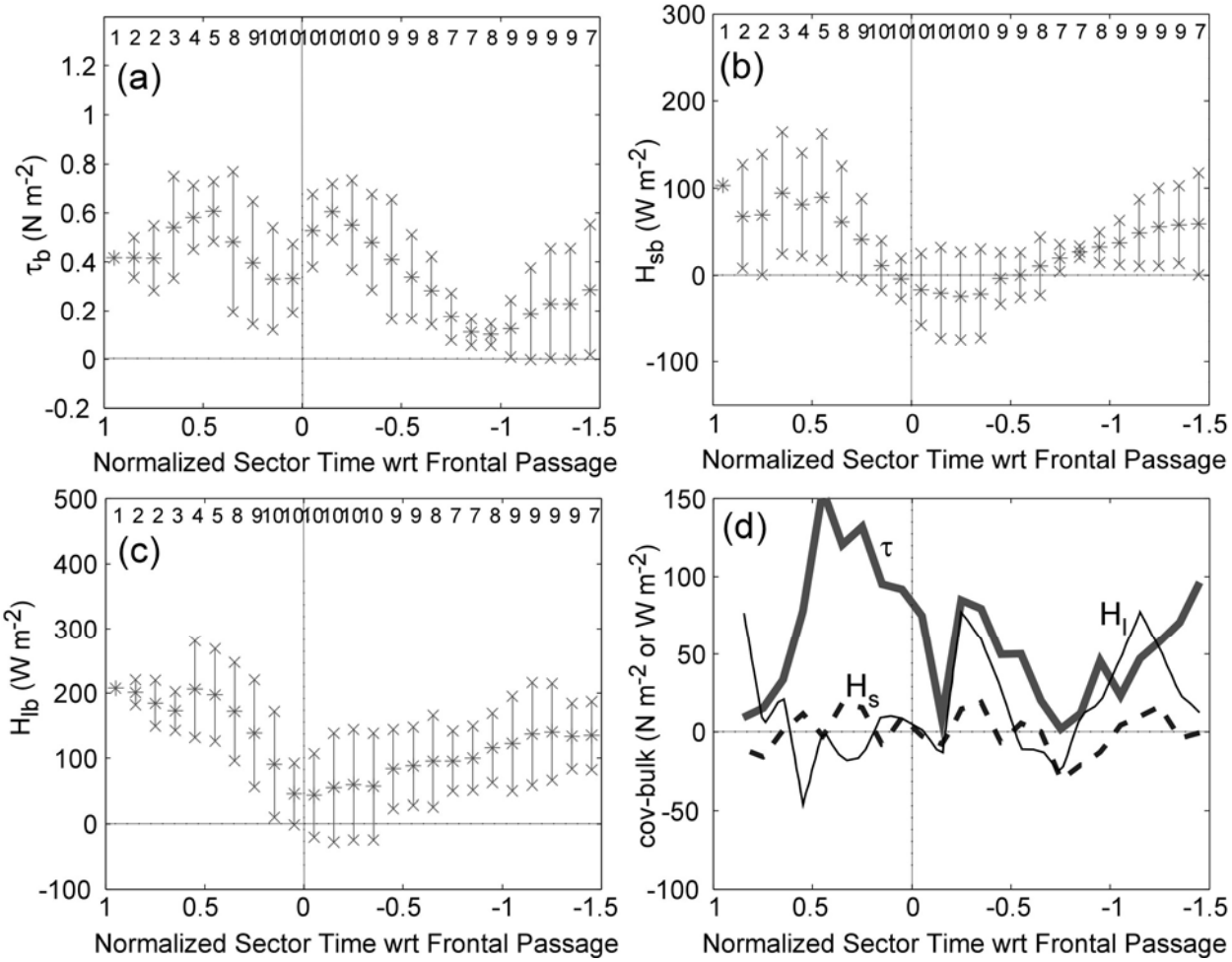

Figure 18. Composites of (a) stress, (b) sensible heat flux, and (c) latent heat flux calculated from the bulk formulas of Fairall *et al.* (2003). In (d), the differences between the covariance and bulk values of stress (heavy solid), H_s (dash) and H_l (thin solid) are shown. Note that the stress differences have been multiplied by 500 to scale properly on the plot.

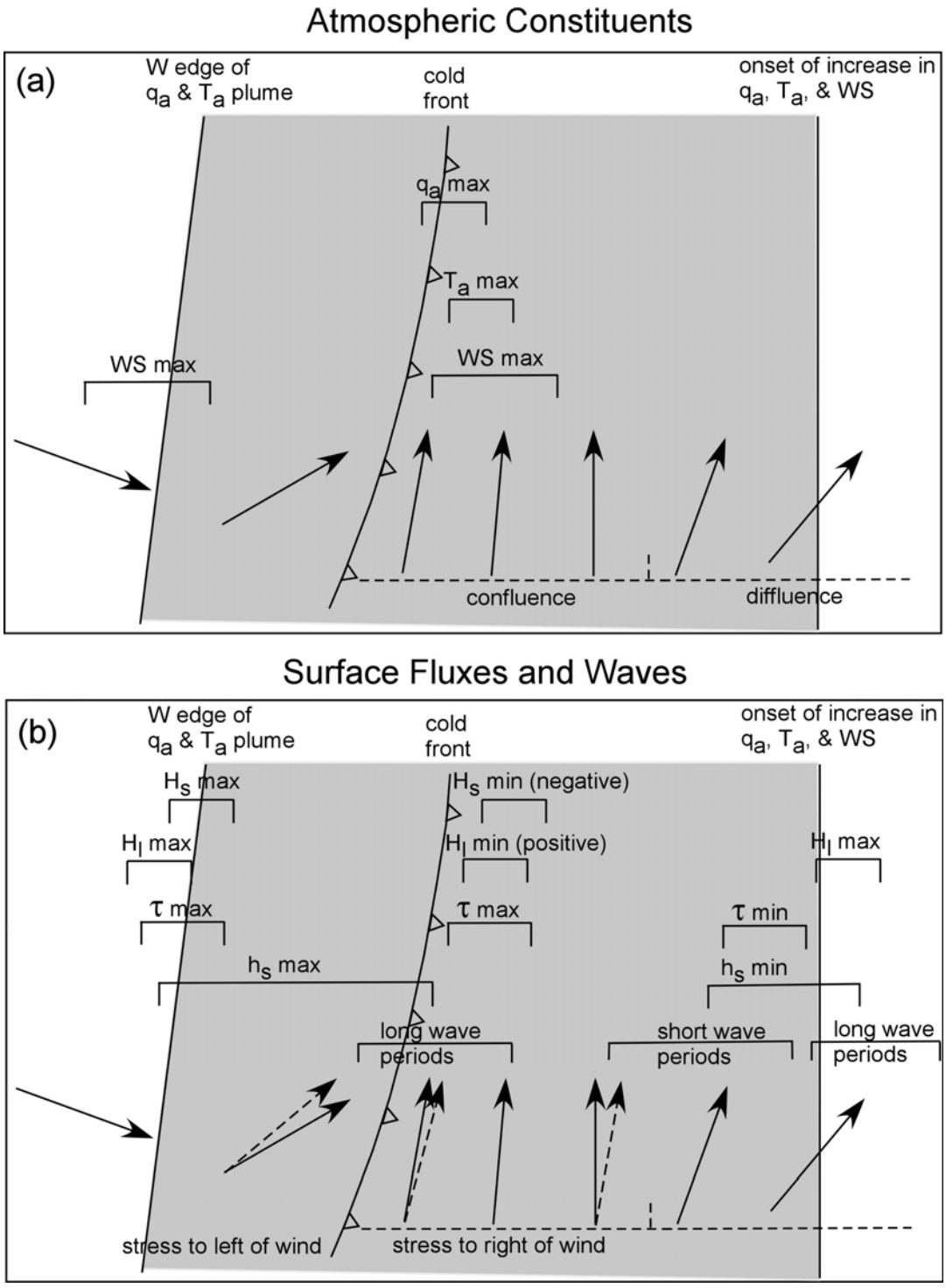

Figure 19. Schematic diagram summarizing the composite variations of (a) the atmospheric constituents, and (b) the surface fluxes and ocean waves relative to the warm sector, cold front, and post-frontal regions. T_a, q_a, WS, H_s, H_l, τ, and h_s represent atmospheric temperature, atmospheric water vapor, wind speed, sensible heat flux, latent heat flux, stress, and significant wave height, respectively. The solid arrows show wind direction and the dashed arrows in (b) show stress direction. The region representing the atmospheric water vapor plume is shaded.